The Spatial Atlas of Human Anatomy (SAHA): A Multimodal Subcellular-Resolution Reference Across Human Organs

Jiwoon Park[1,2], Roberto De Gregorio[1,3], Erika Hissong[1,4], Elif Ozcelik[1], Nicholas Bartelo[1], Felipe Segato Dezem[5,13], Luke Zhang[5,6], Maycon Marção[5,6], Hannah Chasteen[5,6], Yimin Zheng[7], Ernesto Abila[7,8], Junbum Kim[1], Theodore Nelson[1], Jacqueline Proszynski[1], Akua A. Agyemang[1], Mohith Reddy Arikatla[1], Arjumand Wani[5,6], Yutian Liu[5,6], Evelyn Metzger[9], Stefan Rogers[9], Prajan Divakar[9], Parambir S. Dulai[10,11], Jason Reeves[9], Yan Liang[9], Liuliu Pan[9], Sayani Bhattacharjee[9], Michael Patrick[9], Kimberly Young[9], Ashley Heck[9], Mithra Korukonda[9], Dan McGuire[9], Lidan Wu[9], Aster Wardhani[9], Joseph Beechem[9], George Church[2], Steven M Lipkin[1], Aaron Berliner[1], Sanjay Patel[1,4], Fabio Socciarelli[1,4], Jan Krumsiek[1,3], Rohit Chandwani[1], Sebastien Monette[12], Brian Robinson[1,4], Massimo Loda[1,4], Olivier Elemento[1,3], Luciano Martelotto[13,*], Jasmine Plummer[5,6,14,15,*], André F. Rendeiro[7,8,*], Alicia Alonso[1,3,*], Robert E. Schwartz[1,*], Shauna Lee Houlihan[1,3,], Christopher E. Mason[1,*]

Affiliations:
[1] Weill Cornell Medicine, New York, NY, USA
[2] Harvard Medical School, Boston, MA, USA
[3] Caryl and Israel Englander Institute for Precision Medicine, Weill Medical College of Cornell University, New York, USA
[4] Department of Pathology and Laboratory Medicine, Weill Medical College of Cornell University, New York, NY, USA
[5] Center for Spatial Omics, St. Jude Children's Research Hospital, Memphis, TN, USA
[6] Department of Developmental Neurobiology, St. Jude Children's Research Hospital, Memphis, TN, USA
[7] CeMM Research Center for Molecular Medicine of the Austrian Academy of Sciences, Vienna, Austria
[8] Ludwig Boltzmann Institute for Network Medicine at the University of Vienna, Austria
[9] Bruker Spatial Biology, Seattle, WA, USA
[10] Department of Medicine, Division of Gastroenterology and Hepatology, Northwestern University Feinberg School of Medicine
[11] Center for Human Immunobiology, Northwestern University Feinberg School of Medicine
[12] Memorial Sloan Kettering Cancer Center, New York, NY, USA
[13] University of Adelaide, Adelaide, Australia
[14] Comprehensive Cancer Center, St. Jude Children's Research Hospital, Memphis, TN, USA
[15] Department of Cellular & Molecular Biology, St. Jude Children's Research Hospital, Memphis, TN, USA

*Corresponding author(s): L.M., J.T.P., A.F.R., A.A., R.E.S., S.L.H., C.E.M.; Main contact: Christopher E. Mason (chm2042@med.cornell.edu)

ABSTRACT

The Spatial Atlas of Human Anatomy (SAHA) represents the first multimodal, subcellular-resolution reference of healthy adult human tissues across multiple organ systems. Integrating spatial transcriptomics, proteomics, and histological features across over 15 million cells from more than 100 donors, SAHA maps conserved and organ-specific cellular niches in gastrointestinal and immune tissues. High-resolution profiling using CosMx SMI, 10x Xenium, RNAscope, GeoMx DSP, and single-nucleus RNA-seq reveals spatially organized cell states, rare adaptive immune populations, and tissue-specific cell-cell interactions and ligand-receptor pairs. Comparative analyses with colorectal cancer and inflammatory bowel disease demonstrate the power of SAHA to detect disease-associated spatial disruptions, including crypt dedifferentiation, perineural invasion, and therapy-resistant immune remodeling. All data are openly accessible through a FAIR-compliant interactive portal to support exploration, benchmarking, and machine learning model training. Through SAHA, we provide a foundational framework for spatial diagnostics and next-generation precision medicine grounded in a comprehensive human tissue atlas, enabling the development of context-aware models that simulate tissue behavior, decode complex pathologies, and accelerate therapeutic innovation at unprecedented scale.

INTRODUCTION

Human tissues normally maintain structural integrity and function across diverse physiological states, but how these architectures break down in disease, aging, and stress remains a fundamental, largely unresolved question in biology and medicine. The advent of spatial omics technologies has transformed our ability to map gene and protein expression within intact tissues, offering subcellular-resolution insights into cellular interactions and tissue architecture [1,2]. Yet a critical gap remains: there is no comprehensive spatial reference of healthy human tissues across multiple organ systems. While existing atlases like the Human Cell Atlas [3], Human Protein Atlas, and Human Tumor Atlas Network [4], have advanced our understanding of single-cell biology, they are largely derived from dissociated cells or disease-specific samples, limiting their utility as healthy spatial baselines [5].

To address this critical need [6], we established the Spatial Atlas of Human Anatomy (SAHA)—the first multimodal, subcellular-resolution reference atlas of healthy adult human tissues spanning gastrointestinal and immune systems. SAHA integrates spatial transcriptomic, proteomic, and histological data from over 100 diverse donors, capturing cellular organization at ~50 nm resolution. Unlike prior efforts, SAHA implements a rigorously standardized pipeline for tissue procurement, processing, quality control, and cross-platform integration. Our initiative enables consistent and reproducible analysis across organs, individuals, and spatial profiling technologies, while preserving the architectural context often lost in dissociated single-cell studies.

SAHA not only provides a high-resolution baseline of normal tissue organization but also facilitates comparative analyses with diseased tissues, enabling identification of spatially defined pathologies such as immune-epithelial remodeling, crypt dedifferentiation, and rare

invasive niches. Through an open-access, FAIR-compliant [7] data portal (link to be updated upon acceptance), SAHA aims to serve as a foundational benchmark for translational research, computational modeling, and spatially informed diagnostics [8].

Here, we report the first phase of SAHA encompassing 16 gastrointestinal and immune tissue types and demonstrate its utility for spatially resolved analysis of diseases, such as colorectal cancer, pancreatic cancer, and inflammatory bowel disease. SAHA represents the largest subcellular resolution, multimodal transcriptomic and proteomic dataset of healthy human tissues to date, enabling the characterization of both conserved and organ-specific spatial niches. Through comparative analyses with diseased cohorts, we illustrate SAHA's translational potential as a reference framework for identifying pathological alterations. By bridging spatial molecular profiling with clinical precision medicine, SAHA establishes a new paradigm for functional tissue atlas and a blueprint for the next generation of spatial omics research.

RESULTS

1. Overview of the first gastrointestinal and immune spatial organ atlas

The first phase of the Spatial Atlas of Human Anatomy (SAHA) systematically mapped major digestive and immune organs at subcellular resolution, capturing over 15 million cells from over 100 healthy adult donors (ages 27-81 years, **Supplementary Table 1**). Using multiple high-plex spatial platforms including CosMx™ Spatial Molecular Imager, Xenium, RNAscope™, and GeoMx® Digital Spatial Profiler, we captured high-resolution profiles of stomach, liver, pancreas, small intestine (ileum), large intestine (descending colon and appendix), bone marrow, and lymph nodes. To provide a molecular bridge between spatially resolved tissue architecture and a more readily available clinical sample type, we also included peripheral blood mononuclear cells (PBMCs), which represent a non-solid tissue component (**Fig. 1, Supplementary Table 2**). We profiled 15,915,616 cells, including 9.5 million tissue-resident cells and 6 million circulating blood cells, at a spatial resolution of 50 nanometers. For the normal reference tissues, the CosMx RNA (1000-plex) dataset included 94 tissue samples, profiling 2.9 million cells and capturing over 524 million individual transcript measurements. This 1000-gene spatial atlas represents a substantial advancement in transcriptomic resolution—enabling detailed cell type phenotyping and cell–cell interaction analysis while preserving subcellular spatial fidelity. The corresponding CosMx protein dataset (67-plex) profiled 3.5 million cells and yielded over 17.8 billion quantified protein features. In contrast, disease and PBMC samples were analyzed using expanded RNA panels (6000-plex or 19,000-plex), providing deeper molecular coverage for characterizing rare populations and disease-specific states.

Standardized tissue collection and rigorous quality control were implemented to minimize batch effects and cross-platform variability, ensuring robust data integration and downstream analysis [9] (See **Methods**, **Extended Data Fig. 1, Supplementary Table 2**). This enabled joint analysis of transcriptomic profiles across organs, revealing both conserved and organ-specific cellular identities. Uniform Manifold Approximation and Projection (UMAP) of combined CosMx RNA data demonstrated distinct clustering of major epithelial lineages—such as hepatocytes (liver),

acinar and ductal cells (pancreas), and gastric parietal and chief cells (stomach)—alongside broad immune populations including T cells, B cells, macrophages, and dendritic cells (**Fig. 2a, Extended Data Fig. 2a**). In total, over 50 distinct cell types were annotated using canonical marker genes, encompassing broad epithelial, immune, stromal, and neuronal lineages, highlighting both conserved and organ-specialized programs of cellular diversity and relative abundance (**Fig. 2b-d**).

Subcellular resolution enabled precise localization of transcripts and proteins within individual cellular compartments, allowing us to map the anatomical distribution of billions of biomolecules (RNA transcripts and proteins) across tissue sections. While higher resolution can increase technical variability and noise, our quality control strategy (i.e., histopathological review, quantification of control probes, RNAscope-based RNA integrity assessment, and platform cross-validation) ensured robust reproducibility across tissues and donors (**Extended Data Fig. 3**). For example, RNAscope control probes (i.e., *PPIB*) benchmarked RNA quality, and Spearman correlation analyses demonstrated a strong monotonic relationship ($\rho = 0.86$, p-value = 0.0007) between RNAscope and CosMx transcript measurements, with no detected systematic bias, while CosMx maintained greater transcriptome coverage due to its higher plex capacity (**Extended Data Fig. 3a-c**). Together, these analyses establish the technical reproducibility and biological validity of SAHA datasets and cell annotations, enabling robust cross-organ and cross-platform comparisons and providing a reliable reference for future spatial studies. Quality metrics across sample cohorts were highly consistent (**Extended Data Fig. 3d**), underscoring the robustness of the integrated data resource. This inaugural phase of SAHA establishes the largest high-quality, multimodal spatial reference of the human digestive and immune systems at subcellular resolution—providing a foundational resource for investigating tissue architecture, cellular diversity, and microenvironmental organization in health and disease.

2. Cellular neighborhoods and interactions across intestinal and immune structures

Leveraging an integrated embedding of over 15 million spatially profiled cells, SAHA enables both cross-organ comparisons and high-resolution analysis of spatial architecture within and across organ systems, tissue types, and cell populations (**Fig. 2**). This flexible framework supports multiscale investigation of tissue organization and microenvironmental interactions. In the gastrointestinal system, high-plex spatial profiling revealed nuanced, layer-specific architectures and discrete cellular niches spanning the epithelium and underlying submucosa (**Fig. 3a**). In the colon, for example, epithelial crypts were distinctly segmented, with *PIGR* and *MHC-I* expression localized to mucosal and submucosal regions, and smooth muscle markers (e.g., *ACTA2*) confined to the muscularis layer. Cell-level adjacency mapping further uncovered localized immune infiltration at crypt boundaries, suggesting active epithelial-immune crosstalk that is not readily detectable in dissociated single-cell datasets.

SAHA also provides a topographical link between structure and single-cell activity, wherein analysis of regionally enriched gene programs demonstrated spatial specialization along tissue depth axis (**Fig. 3b**). For example, outer crypt regions were enriched for keratinization-

associated signatures, whereas deeper crypt zones expressed genes involved in antigen-processing and presentation (**Fig. 3b**). Spatial mapping of cell cycle regulators (e.g., *CDKN1A*, *CCND1*) and stress-response genes (e.g., *TFEB*) showed selective enrichment at immune-rich epithelial interfaces, suggesting localized zones of proliferative and immunomodulatory adaptation (**Fig. 3c**). Unbiased clustering of cell-cell adjacency networks further delineated distinct cellular neighborhoods across crypt and submucosal compartments (**Fig. 3d-f**). Discrete microenvironments dominated by epithelial cell to T cells, B cells, or myofibroblast interactions emerged along the crypt-luminal axis, emphasizing substantial spatial heterogeneity even within morphologically similar layers. These findings further highlight the unique ability of subcellular-resolution spatial profiling to uncover microanatomical, structural features that are inaccessible through dissociated single-cell approaches.

Beyond crypt-associated immune niches, gastrointestinal organs also revealed highly organized lymphoid structures. In the appendix (**Fig. 3g, Extended Data Fig. 4**), we identified large lymphoid aggregates composed of interspersed T and B cells surrounded by mesenchymal and myeloid populations. Force-directed graph visualizations of cell-cell adjacency networks demonstrated dense immune-immune interactions within these aggregates, consistent with their role as specialized hubs for adaptive immune activation (**Fig. 3h**). UMAP embeddings annotated by both broad and fine-grained cell identities highlighted tight spatial co-localization of functionally distinct immune subsets, including T follicular helper cells and germinal follicle center B cells (**Fig. 3i**). Ligand-receptor interaction analyses further revealed frequent paracrine signaling among these populations, suggesting coordinated immunological activity within these spatially confined niches (**Fig. 3j**).

These lymphoid aggregates occupy anatomically defined regions within gastrointestinal tissues and serve as sites of antigen presentation, lymphocyte activation, and localized immune coordination. To assess the generalizability of such spatially organized immune niches, we compared them with canonical germinal centers (GCs) in lymph nodes (LNs). Unsupervised clustering and spatial mapping of LN datasets revealed distinct compartmentalization between GC-resident B cells and surrounding immune and stromal populations (**Fig. 4a, Extended Data Fig. 5a-b**). Differential expression analysis further highlighted this organization, with B cell and antigen presentation genes (e.g., *CD74*, *CD79A, HLA-DRA*) enriched in GC cores (q-values = 5.47×10^{-34}, 1.89×10^{-10}, 1.20×10^{-20}), while stromal and chemotactic transcripts (*CCL21, CXCL12, VIM*) localized to adjacent zones (q-values = 3.18×10^{-99}, 7.21×10^{-24}, 4.84×10^{-20}) (**Extended Data Fig. 5c-f**).

To compare gut-associated lymphoid structures with canonical germinal centers, we analyzed anatomically paired epithelial (APE) lymphoid aggregates in the gastrointestinal tract. Similar to lymph node GCs, intra-GC B cells in APE structures expressed *IGHG1* and *IGKC*, while surrounding stromal regions were enriched for *APOE* and extracellular matrix genes (**Fig. 4c, Extended Data Fig. 5g**). However, unlike the sharply zonated architecture of lymph nodes, APE lymphoid structures were embedded within a more intermixed environment of epithelial and mesenchymal cells (**Fig. 4d-e**), suggesting greater potential for varied immune-epithelial crosstalk. Moreover, the SAHA data showed both generalized and tissue-specific transcriptomic

gradients across GC and peri-GC regions in LN versus APE, highlighting organ-specific spatial organization (**Extended Data Fig. 5h**).

Expanding our analysis across all SAHA gastrointestinal tissues—including appendix (APE), ileum (ILE), colon (COL), and stomach (STO)—we profiled 43 patient samples comprising 948 fields of view (FOVs) and over 1.15 million spatially resolved cells (**Fig. 4g**). Integrative clustering of transcriptomic profiles combined with spatial adjacency information identified three major niche types: (1) organ-shared epithelial-immune interaction zones, (2) organ-specific immune microenvironments within lymphoid structures, and (3) rare cell populations with distinct spatial distributions (**Fig. 4h-k, Extended Data Fig. 6**). Notably, shared epithelial-immune neighborhoods, characterized by dense T- and B-cell infiltration adjacent to crypt structures, were recurrently observed in both colon and ileum samples (**Fig. 4h-i, Extended Data Fig. 6a-d**). In contrast, the stomach exhibited parietal-chief cell clusters unique to gastric glands, and the appendix contained specialized adaptive immune hubs, reflecting tissue-specific adaptations of immune-epithelial architecture (**Fig. 4j-k**).

To investigate the functional roles of these spatial niches, we leveraged the unique ability of spatial data to profile the ligand-receptor interaction networks between shared and organ-specific microenvironments. Conserved immune-epithelial niches were dominated by paracrine signaling between compartments, whereas tissue-specific structures exhibited distinct adaptive immune signaling profiles (**Extended Data Fig. 6e**). In addition, complementary spatial variance analysis revealed that genes involved in immune activation (e.g., *CD74*, *IGHM*), epithelial barrier integrity (e.g., *PIGR*), and chemokine signaling (e.g., *CCL21*) were highly localized within discrete spatial clusters (**Fig. 4l**). These findings suggest that spatial neighborhoods are defined not only by their cellular composition but also by localized transcriptional programs and interactions. Collectively, these analyses demonstrate that spatial information is essential for uncovering hierarchical tissue organization, functionally specialized microenvironments, and organ-specific immune architecture in the human gastrointestinal tract.

3. Validation and integration of multimodal spatial data

The detailed spatial mapping of gastrointestinal tissues highlights the power of subcellular-resolution atlases to uncover structured microenvironments and immune-epithelial interactions. To ensure the robustness and biological fidelity of these insights across platforms and tissues, we systematically validated SAHA datasets through multimodal integration of spatial transcriptomic and proteomic data. More importantly, we performed cross-platform validation using several orthogonal spatial assays, including CosMx RNA and protein profiling, 10x Genomics Xenium, RNAscope, GeoMx DSP, and histopathology-based annotations (**Supplementary Table 2**).

Integration of CosMx RNA and protein data enabled single-cell-level validation of biological consistency and facilitated deeper characterization of cell states and subtypes. Co-embedding of 1000-plex CosMx RNA and 67-plex CosMx protein profiles preserved tissue structure and cellular identities, confirming the robustness of multimodal spatial profiling (**Fig. 5a, Extended**

Data Fig. 7a-b). Canonical markers such as CD45 (PTPRC), E-cadherin (CDH1), CD3D, and CD20 (MS4A1) exhibited concordant expression across RNA and protein modalities (**Fig. 5b-d**). Protein-based annotations aligned closely (Adjusted Rand Index, ARI = 0.2719) with RNA-integrated labels using Maxfuse [10], supporting consistent cell type classification across modalities and batches (**Fig. 5c, Extended Data Fig. 7c-d**). Protein data also provided clearer delineation of architectural features, such as the epithelial-stromal interface in the stomach and lymphoid aggregates in the appendix (**Fig. 5d**), reflecting the stability, localization, and abundance of structural proteins relative to transcriptomic signals [11]. However, the transcriptomic profiles offered broader molecular coverage (up to 19k probes vs. <100 protein targets), enabling finer discrimination of epithelial subtypes and detection of rare populations such as stem and transit-amplifying cells.

Beyond validating cell identity and tissue structure, protein datasets offer orthogonal confirmation of receptor-ligand interactions inferred from RNA data (**Fig. 5e**) and provide direct evidence of translational activity. While such multimodal comparisons reinforce biological interpretation, it is important to note that RNA-protein correlations are not always linear, nor should it always be. Although this discordance has been examined for decades, systematic large-scale comparisons with subcellular resolution have remained limited [12,13]. Leveraging SAHA's multimodal and high resolution (50 nm), we directly compared matched RNA and protein measurements across multiple organs (**Fig. 5f**). Housekeeping and structural genes such as VIM showed strong concordance (adjusted R-squared of more than 0.5), whereas key immune and signaling molecules—including RELA and IGHD—displayed substantial discrepancies between RNA and protein levels (adjusted R-squared of less than 0.1) (**Fig. 5f, Extended Data Fig. 7e-f**). These differences were further highlighted in cross-organ analyses: VIM exhibited consistent RNA-protein correlation across tissues (R^2 = 0.5781 with p-value = 0.0026 when compared across all SAHA cells), whereas IL1B showed widespread RNA expression with minimal protein detection. Conversely, CD276 demonstrated robust protein abundance despite low transcript levels, consistent with post-transcriptional regulation [14]. These comparisons underscore the necessity of multimodal profiling to accurately capture both transcriptional potential and protein-level function.

The integration of histopathology-based annotations with spatial molecular profiles reinforced biological interpretability and enabled precise mapping of anatomical features to molecular states. Histological landmarks such as crypt architectures, lymphoid aggregates, and smooth muscle layers corresponded closely (qualitatively evaluated by cell types and niche clusters) labeled to spatial clustering patterns observed in molecular datasets (**Fig. 6**). This alignment between morphology and molecular identity validates the technical robustness and biological fidelity of the SAHA datasets, supporting consistent cross-tissue, cross-platform, and cross-modality analyses at subcellular resolution.

To further harness histological information, we applied CONCH, a multi-modal vision-text foundation model [15] that decodes tissue architecture from hematoxylin and eosin (H&E) stained whole-slide images (**Fig. 6a-b**). The model extracts quantitative morphological features from image tiles and learns spatial embeddings, which preserve anatomical continuity and

discriminate between distinct structural zones (See **Methods**, **Fig. 6c-d**). Unsupervised (leiden) clustering of these image-derived features reconstructed tissue organization, including epithelial boundaries, stromal interfaces, and muscular layers (**Fig. 6e**). Visualization of representative clusters using UMAP revealed discrete and biologically meaningful groupings that corresponded to histologically distinct morphotypes, such as crypt bases, glandular epithelium, and lymphoid-rich regions most of which aligned with unbiased, RNA-based spatial clustering results (**Fig. 4g-k, 6f**).

This approach generalizes across gastrointestinal tissues, as image-derived embeddings from the colon, ileum, and appendix consistently showed conserved morphological classes, including crypt epithelium, extracellular matrix, and immune niches (**Fig. 6g**). Morphological clusters overlapped with specific histopathological terms scored by the multi-modal vision-text model (**Fig. 6h**) and displayed enrichment for specific tissue compartments such as epithelial, connective, or immune components (**Fig. 6i**). Spatial adjacency patterns among clusters (**Fig. 6j**) and their correlations with RNA-derived cell type proportions (**Fig. 6k**) further confirmed that image-derived features captured biologically relevant gradients in tissue organization. Finally, direct comparison of H&E image and CosMx RNA projection revealed highly consistent alignment shown by positive CCA correlation, between image-based morphology and transcriptomically defined cell types (**Fig. 6l**), illustrating the power of histology-informed molecular modeling for spatial atlas construction.

4. SAHA's utility and impact in biomedical research

A key motivation for constructing SAHA was to enable comparative spatial analysis of diseased tissues, particularly in contexts where matched healthy controls are unavailable. To demonstrate its translational utility, we applied SAHA to two clinically relevant diseased conditions: colorectal cancer (CRC) and inflammatory bowel disease (IBD).

Using CRC samples, we analyzed transcriptional and structural profiles in tumor adjacent crypt regions and compared healthy tissue (SAHA COL, $n = 3$) to histologically normal crypts from CRC resections ($n = 1$) (**Fig. 7a**). Crypt regions were stratified and annotated as 'top' and 'bottom' crypts, based on gene expressions and their locations (**Fig. 7b, Extended Data Fig. 8a-b**). Bottom crypts were identified by enrichment of genes associated with intestinal stem cells (*OLFM4*) and differentiated secretory cells (*LEFTY1, STMN1*), whereas top regions expressed mature epithelial markers (e.g., *KRT20, PLAC8, CEACAM1*). Notably, crypts adjacent to CRC exhibited disruption in spatial expression patterns; markers normally restricted to bottom regions (i.e., *H2AZ1, SPINK1*) were aberrantly expressed in the upper crypts, and vice versa for *CEACAM6* and *CEACAM1* (**Fig. 7c, Supplementary Table 3**). These patterns potentially indicate crypt dedifferentiation and spatial disorganization often associated with tumor formation [16,17].

Tumor-adjacent crypts showed widespread changes in gene expression, with significantly more genes up- or down-regulated compared to healthy crypts (**Fig. 7c**). Several upregulated genes, including *REG1A*, have been previously associated with poor prognosis and crypt-inflammation

in CRC, while upregulation of *IL6* and *IL22* receptors are known to promote inflammation and tumor development in CRC [18,19]. CRC-associated crypts had a substantially higher number of differentially expressed genes (DEGs) compared to COL crypts, indicating broader transcriptional reprogramming (i.e., 96 vs 61 DEGs in bottom crypt and 116 vs. 72 DEGs in top crypt; **Supplementary Table 3**). In terms of the tumor microenvironment, FOVs profiled from CRC samples showed a significant increase in the number of mast cells (**Extended Fig. 9c**), a known driver of angiogenesis and metastasis [20].

To further investigate spatial expression and organization of RNA transcripts, we performed spatial autocorrelation analysis using Moran's I and clustered FOVs based on their top 200 spatially variable genes (SVGs) (**Fig. 7d**). This unsupervised approach effectively distinguished crypts from CRC and COL samples, indicating their divergent spatial states. From matched top and bottom crypt compartments across conditions, we visualized all SVGs and identified both conserved spatial markers (e.g., *KRT20, CEACAM1, CEACAM6*) and spatially enriched disease-associated genes (e.g., *REG1A, IL22RA1*) - both of which were also noted in our differential expression analysis (**Fig. 7e-f, Extended Data Fig. 8e**).

Beyond structural comparisons, SAHA enabled exploration of intrapatient tumor heterogeneity (**Fig. 7g-j**), including rare events such as perineural invasion (PNI) (**Fig. 7k-m**). Within a single CRC sample, we identified two spatially and transcriptionally distinct tumor subtypes (labelled as Type 1 and Type 2), based on dominant cell compositions and immunogenicity (**Fig. 7g**). Type 1 tumor regions exhibited a higher lymphocyte to tumor ratio with increased proportions of cytotoxic and naive CD8+ T cells, whereas Type 2 regions were enriched for macrophage subsets (**Fig. 7g-j, Extended Data Fig. 8f-g**).

We captured a rare perineural invasion event among the analyzed FOVs, characterized by dysplastic stroma surrounding a nerve and tumor cells encircling the perineurium (**Fig. 7k**). Although perineural invasion is recognized as a hallmark of aggressive CRC, it remains difficult to resolve with conventional histopathology and immunofluorescence, which lack comprehensive transcriptomic resolution [21–23] . While recent single-cell RNA-seq studies have attempted to profile these events, they often fail to capture neural cells altogether—or, if captured, cannot confidently localize them or distinguish whether they are part of a PNI structure or simply present in unrelated regions of the tissue [24–26]. By leveraging the spatial context of SAHA, we subclustered this PNI region and uncovered a rare subset of fibroblasts (less than 100 cells in the PNI region) in close proximity to glial cells, characterized by a hybrid transcriptional signature expressing both glial-associated genes (*CLU, NGFR, SLC2A1, APOD*) and cancer-associated fibroblast markers (<2% of fibroblasts identified in the sample) such as *CXCL14* and *MMP2* [27,28] (**Fig. 7k-l, Extended Data Fig. 8h**). Cell-cell communication analysis further revealed unique signaling pathways within the PNI niche, including the ANGPTL pathway originating from fibroblasts, previously associated with increased metastatic risk in CRC [29–31], and the LIFR pathway, exclusively signaling from tumor cells to glial cells, known to facilitate tumor-fibroblast crosstalk and activate pro-invasive programs [32]. These findings offer new insights into the interactive dynamics within this rare microenvironment and its ability to specify high resolution details of rare tumor types.

We also compared SAHA ILE with ileal samples from patients with inflammatory bowel disease (IBD), including individuals stratified by clinical response to TNFα inhibitor therapy (**Fig. 8a**). Integration of CosMx RNA profiles across healthy and IBD ileum samples revealed clear separation by disease state, while preserving major cell type identities (**Fig. 8b, Extended Data Fig. 9a-b**). Correlation analysis of average gene expression profiles demonstrated strong consistency (e.g., spearman correlation R^2 of 0.74 for epithelial cells from 1K and 6K datasets) across datasets generated with different plex sizes, validating the reproducibility of cell-type transcriptional programs (**Extended Data Fig. 9a**). Spatial mapping of cell types demonstrated increased immune cell infiltration into epithelial compartments in IBD samples relative to healthy controls (**Fig. 8c, Extended Data Fig. 9c-d**).

Quantification of epithelial-proximal immune infiltration within 300 μm confirmed a significant increase in immune cell density in IBD tissues ($p < 0.001$; **Fig. 8d**). Ligand–receptor interaction analyses further revealed enhanced immune-epithelial signaling in IBD, particularly among non-responders to TNFα therapy, who exhibited elevated spatial interaction scores relative to responders (**Fig. 8e**). Mesenchymal-stromal populations in IBD tissues showed increased expression of pro-inflammatory and extracellular matrix remodeling markers, including elevated *TNFRSF1A* (TNF receptor 1) expression among non-responders compared to responders ($p < 0.05$; **Fig. 8f**). Spatial mapping of TNF-TNFRSF1A ligand–receptor interactions localized active signaling to immune-mesenchymal interfaces, particularly in non-responder tissues (**Fig. 8g**).

Moreover, these molecular level changes were consistent with the histological analyses. As performed for the healthy GI tract (**Fig. 6**), we applied a multi-modal text-vision model to quantify and describe the morphological patterns of H&E-stained ileum sections of healthy and IBD tissues (**Fig. 8h**). IBD samples were distinguishable from healthy, with histopathological terms related to metaplasia, immune cell infiltration, crypt branching, and apoptosis more frequent in IBD samples compared to controls (**Fig. 8i**). Furthermore, we also found differentially enriched morphological changes in response to TNFα treatment (**Fig. 8i**), which were aligned with molecular findings, reinforcing the multi-layered disruption of epithelial and stromal architecture in IBD [33]. These analyses demonstrate how SAHA enables spatially resolved comparisons of healthy and diseased tissues at both molecular and histological levels, providing critical insights into disease-associated microenvironmental changes and therapeutic response heterogeneity.

The integration of spatial transcriptomics and proteomics extends the analytical frameworks traditionally applied to single-cell sequencing by adding critical layers of structural and contextual information (**Fig. 9a**). Spatial multi-omics enables not only transcriptomic and proteomic profiling at subcellular resolution, but also the characterization of extracellular matrix (ECM) features, direct cell-cell interactions, and subcellular biomolecule localization, which are dimensions inaccessible to dissociated single-cell methods. The addition of spatial context enables direct measurement of cellular phenotypes, resolving the challenge of drawing conclusions from disconnected data. This multidimensional mapping redefines efforts in building biological atlases and opens new avenues for understanding tissue organization and function.

Recent technological advances now enable high-throughput, same-cell spatial multi-omics at subcellular resolution—capturing whole-transcriptome RNA (~19,000 genes), high-plex protein expression (~67 markers), and histological context within a single assay (**Fig. 9a**). These spatial platforms also provide cell morphology, boundary, and segmentation data that are inaccessible via traditional dissociated single-cell methods. To scale this approach across large tissue volumes and billions of cells, we implemented computational workflows capable of integrating transcriptomic, proteomic, and H&E morphological data at population scale. Compared to conventional scRNA-seq, spatial multi-omics approaches using Xenium and CosMx offer orders-of-magnitude lower cost per cell and support efficient scaling to billions of cells with fewer experimental runs—facilitating population-scale spatial atlasing (**Fig. 9b**).

To maximize accessibility and impact, SAHA adheres to the FAIR (Findable, Accessible, Interoperable, and Reusable) data principles. The SAHA data portal provides an open-access platform for exploring spatial multi-omics datasets, equipped with interactive visualization tools, high-resolution tissue navigation, and download capabilities for downstream analysis (**Fig. 9c**). Beyond serving as a reference, SAHA establishes standardized protocols and integration frameworks that can be adopted across institutions to enable scalable, reproducible spatial profiling.

DISCUSSION

The Spatial Atlas of Human Anatomy (SAHA) establishes the first multi-organ, multimodal, and multi-platform reference map of healthy human gastrointestinal and immune systems at subcellular resolution, providing a foundational resource for investigating tissue architecture, cellular diversity, and microenvironmental organization for healthy and diseased states. By integrating histological, proteomic, and transcriptomic data across tissues and spatial technologies, SAHA addresses major limitations of previous atlasing efforts, which have predominantly relied on dissociated single-cell data and lacked spatial context. A key strength of SAHA lies in its rigorously standardized experimental and computational pipelines, which ensure reproducible, high-quality data generation and facilitate integrative analyses across organs and modalities. To support cross-platform consistency, we implemented systematic validation across CosMx, Xenium, GeoMx, and RNAscope platforms, alongside robust quality control metrics. While SAHA initially leveraged 1000-plex RNA profiling, we also introduce, to our knowledge, the first whole-transcriptome and paired protein multi-omics datasets at subcellular resolution—expanding beyond mid-plex spatial transcriptomics to unlock deeper biological insights and establish a future-ready reference for spatial biology.

A central innovation of SAHA lies in its multimodal design and backwards (H&E)-and-forwards (full transcriptome) compatible framework. The integration of RNA, protein, and histopathological (H&E) data facilitates both cross-validation of molecular signals and nuanced dissection of tissue structure and function. This multimodal synergy enabled identification of conserved spatial niches, lineage-specific expression gradients, and regionally restricted cell states, including rare and adaptive immune populations such as follicular B cells and

intraepithelial lymphocytes. We also uncovered fine-grained epithelial and stromal subtypes, such as tuft and enterochromaffin-like cells, and delineated spatially encoded state transitions within common lineages—patterns that would be obscured in single-modality or dissociated datasets. Some segmentation ambiguity is inevitable in a subset of cells, in part due to the physical limitations of tissue sectioning through three-dimensional structures. However, we observe that such instances actually encode meaningful biological information, as spatial proximity—retained in intact tissue—offers a critical dimension absent in single-cell suspensions. Dissociation-based workflows may also lose spatially tethered subpopulations during washing and library preparation steps. While future pixel-level or nucleus-aware segmentation methods [34,35] may refine these boundaries, our current analysis emphasizes broader tissue-level organization, highlighting reproducible spatial relationships that extend beyond cell-intrinsic expression.

Across gastrointestinal tissues—including appendix, ileum, colon, and stomach—SAHA captures a conserved layered organization spanning mucosa, submucosa, muscularis externa, and serosa. At the same time, SAHA reveals organ-specific features, such as crypt-villus gradients, lymphoid aggregates (e.g., Peyer's patches), and vascular-rich stromal zones. These features were consistent across individuals and histologically validated, reinforcing the atlas's technical fidelity. Notably, cross-organ analysis within gastrointestinal tissues uncovered conserved features of mucosal organization while highlighting unique adaptations in the appendix, ileum, colon, and stomach. A comparative profiling of lymphoid aggregates across GI organs and matched germinal centers in lymph nodes revealed both preserved core immune architectures and distinct spatial intermingling with epithelial and stromal compartments, emphasizing the utility of SAHA in decoding tissue-specific immunological microenvironments.

Importantly, SAHA serves not only as a reference but also as an actionable spatial comparator for disease studies—especially in clinical contexts where matched healthy tissue is unavailable. We demonstrate this translational potential by benchmarking SAHA against datasets from colorectal cancer (CRC) and inflammatory bowel disease (IBD). This revealed distinct alterations in crypt top–bottom zonation, immune composition, and spatial gene expression programs. For instance, spatial transcriptomics exposed crypt dedifferentiation in CRC and aberrant cytokine signaling, while perineural invasion—an aggressive metastatic route—was resolved at high granularity, highlighting glia-associated fibroblast states and tumor-nerve signaling circuits. These examples illustrate how SAHA enables spatial biomarker discovery and mechanistic insight into rare or complex pathological events, areas that have been briefly explored in previous studies.

While SAHA represents a significant advance, several limitations remain. First, despite including over 100 donors, our cohort size is modest relative to the full scope of human biological diversity. Further expanding SAHA across age groups, ancestries, and environmental exposures is essential for broader generalizability. Second, although cross-platform integration across CosMx, Xenium, GeoMx, and RNAscope demonstrates strong concordance, inherent technical differences—such as probe capture efficiencies and antibody variability—necessitate ongoing methodological harmonization. Third, this initial phase focuses on gastrointestinal and

lymphoid organs; a complete human reference will require comprehensive coverage across additional anatomical systems.

While the current datasets represent the initial phases of spatial atlas construction, the platform is designed for scalability and community-driven expansion. Active efforts are underway to expand its organ coverage (second phase to genitourinary systems and additional immune organs), apply whole-transcriptome and high-plex proteomics protocols, increase demographic representation, and integrate advanced computational frameworks, including deep learning for tissue segmentation and spatial graph modeling. We also aim to leverage Common Coordinate Framework (CCF)-based registration and analysis pipelines to enable 3D spatial integration across tissue sections and donors. This will support more anatomically precise mapping, facilitate multi-plane reconstruction of tissue architectures, and allow in-depth cross-sample comparisons at scale.

By integrating spatial molecular data with histological and clinical metadata, SAHA provides the infrastructure for building digital twins of human tissues—enabling in silico simulations of disease progression, therapeutic response, cell-cell interactions, and possibly even tissue regeneration. These capabilities position SAHA as a translational bridge between spatial biology and precision medicine, advancing both fundamental research and clinical diagnostics. For example, we can extend SAHA toward perturbation-aware modeling, using spatial benchmarks to assess disease-associated changes and therapeutic responses—analogous to recent large-scale single-cell initiatives such as Tahoe-100M [36]. Together, these directions will transform SAHA into a foundational tool for spatially resolved systems biology and experimental medicine.

The SAHA data portal, built on FAIR (Findable, Accessible, Interoperable, Reusable) principles, will enable broad community access and invite collaborative expansion. We envision that SAHA will not only support basic biological discovery and accelerate clinical translation by providing a standardized framework for the development of spatially informed diagnostics, prognostics, and therapies. As spatial omics technologies continue to evolve, SAHA serves as a dynamic foundation to integrate emerging data types, drive systems-level insights into tissue function and disease, and chart new frontiers in precision medicine. We invite researchers worldwide to utilize SAHA datasets, develop new analytical tools, and contribute additional spatial multi-omics data to collectively accelerate biological discovery and the construction of a comprehensive human spatial atlas.

The integration of SAHA with artificial intelligence frameworks will catalyze a new generation of spatially aware models capable of learning complex tissue organization, molecular gradients, and context-specific cell-cell interactions [37,38]. Unlike dissociated single-cell datasets, SAHA's subcellular-resolution, multimodal profiles retain anatomical fidelity, enabling training of deep learning models that incorporate both spatial topologies, molecular features, and next generation omics. This includes the development of graph neural networks for cell-cell communication inference, foundation models for cross-tissue pattern recognition, and generative architectures for simulating disease progression or therapeutic response within intact tissue contexts. Moreover, SAHA's structured metadata, ontology-linked annotations, and

standardized formats (e.g., AnnData [39], OME-TIFF [40]) make it inherently machine-readable and interoperable across AI pipelines. By coupling biological fidelity with computational scalability, SAHA provides a foundational resource for training AI systems capable of performing high-resolution tissue segmentation, phenotype classification, and predictive modeling across spatial, molecular, and morphological domains.

METHODS

Patient material, ethics approval, and consent for publication

Human tissue samples were obtained from archived formalin-fixed, paraffin-embedded (FFPE) blocks curated by board-certified pathologists and collaborating investigators (**Supplementary Table 1**). Each tissue sample was selected from a diverse ancestry (if possible) from healthy adults (no cancer or organ wide immune issues, ideal age 20-40). If tissues were difficult to get, age and ancestry parameters can be compromised, but no cancer patients or patients with diseases that will cause an impact on not diseased tissues was considered. Representative fields of view (FOVs) were selected following comprehensive histopathological evaluation of H&E-stained slides. All samples were collected under pathology protocols with waivers of consent and authorization.

Tissue microarray (TMA) formalin-fixed, paraffin-embedded (FFPE) blocks were constructed following standard procedures. SAHA FFPE blocks were selected based on histopathological evaluation, and representative areas were identified on hematoxylin and eosin (H&E)-stained slides. Tissue cores (variable in diameter depending on the organ) were extracted using a manual or semi-automated tissue arrayer and transferred into a pre-designed recipient paraffin block. The TMA block was re-embedded and cooled to ensure structural integrity. SAHA FFPE blocks were stored in cardboard boxes at room temperature (RT) under ambient humidity until the day of sectioning.

Tissue processing and histology

The FFPE blocks were sectioned at a thickness of 5 µm, and the sections were placed within Bruker's 15mm x 20mm allowed scan area on Leica Bond Plus slides (Leica Biosystems, S21.2113.A). Fresh ultrapure water was used to fill the water bath and new microtome blades were used for each tissue type. The first few sections from the block face were discarded. The number of serial sections to be collected was determined in advance according to the planned assays. Slides were labeled with a serial number to keep track of the order, ensuring that multiple assays were run on adjacent sections and facilitate subsequent data integration. If needed, one section, usually from the middle of the series, was dedicated to H&E staining, followed by full-slide image acquisition using the Aperio Digital Pathology Slide Scanner system (Leica Biosystems), allowing pathologists to identify and mark the area of interest in consideration of the available number of CosMx fields of view (FOVs). Most sections were also H&E stained after data acquisition. **Supplementary Table 2** lists the serial section numbers for each assay and for the corresponding H&E for each analyzed organ. Following sectioning, the slides were dried upright at RT for 30 minutes (min), followed by a horizontal overnight (ON) drying step at 37°C in an oven to improve tissue adherence. The slides were then stored in a desiccator at RT until processing. Most slides dedicated to the RNA assay were used within two

weeks, as recommended by Bruker. Exact sectioning and run dates are reported in **Supplementary Table 2**.

CosMx processing

Processing of the slides followed the guidelines outlined in the Bruker manuals MAN-10184 for the RNA assay and MAN-10185 for the Protein assay, utilizing the equipment, materials, and reagents recommended in the manuals. Protocol details may have varied over time, reflecting updated manuals throughout the SAHA project. The specific manual version used for each assay is reported in **Supplementary Table 2**.

For the CosMx RNA assay, slides were baked at 60°C ON in vertical position in a baking oven. The following day, CitriSolv (VWR, 89426-268) was used for deparaffinization. Specifically, slides were brought to RT for 3 min, then subjected to two sequential 5 min immersions in CitriSolv, followed by two 5 min washes in 100% ethanol (Et-OH) (Sigma, E7023). The slides were dried vertically for 5 min at 60°C in the same baking oven. Antigen retrieval was conducted in a BioSB® TintoRetriever digital pressure cooker (BioSB, BSB 7015) at 100°C for 15 minutes. After the 5-minute drying step, slides were transferred into the preheated 1X Target Retrieval Solution (part of Bruker 121500006) as per the Bruker manual. The pressure cooker was then closed, and the temperature was allowed to return to 100°C. At this point, a 15 min timer was started, after which the slides were quickly rinsed up and down in DEPC water (Fisher Scientific, BP561-1) at RT for 15 seconds, washed for 3 min in 100% Et-OH, and then dried for 30 min horizontally on a clean surface at RT. 10 min before the end of the drying step, the incubation frame (part of Bruker 121500006) was applied to the slide and a 3 µg/mL Proteinase K (part of Bruker 121500006) working solution in 1XPBS (ThermoFisher Scientific, AM9625) was applied to the sections. The slides were then incubated for 30 min at 40°C in a RapidFISH slide hybridizer oven (Boekel Scientific, 240200). During the final 10 min of digestion, Bruker fiducial beads (part of Bruker 121500006) were resuspended through alternating 1-min vortexing and 2-min sonication steps (three vortexing steps and two sonication steps in total), then diluted in 2X SCC-T (part of Bruker 121500006). Fiducials were diluted at a final working concentration of 0.001% for Appendix, Ileum, Colon, and Pancreas samples, 0.00075% for Stomach and Lymph Nodes samples, and 0.0005% for inflammatory bowel disease ileum samples. Following digestion, slides were washed twice in DEPC water per the manual and then incubated with the prepared fiducials for 5 min, protected from light at RT. The slides were then washed in 1XPBS for 1 min, fixed in 10% Neutral Buffered Formalin (NBF) (EMS Diasum, 15740) for 1 min, washed twice in a 0.1M Tris-Glycine NBF buffer solution for 5 min, once in 1XPBS for 5 min, and incubated with a freshly prepared 100 mM NHS-Acetate (Fisher Scientific, 26777) solution in NHS-Acetate buffer (part of Bruker 121500006) for 15 min in the dark at RT. Finally, the slides were washed twice in 2X SSC (ThermoFisher Scientific, AM9763) for 5 min. At this point, slides were stored in 2X SSC, protected from light, until it was possible to proceed with the ON hybridization step. The required amount of probe for the run was transferred to 0.2 mL tubes, denatured for 2 min at 95°C in a standard thermocycler, and crash-cooled on ice for 1 min. A probe hybridization mix containing RNase inhibitors (Bruker, 121500004) and Buffer R (part of Bruker 121500006) was prepared according to the Bruker manual. Slides were laid horizontally on a clean surface and the hybridization mix was applied to the sections. A plastic coverslip (part of Bruker 121500006) was then placed over the frame. The slides were incubated ON for 17-18 hours (h) at 37°C in the RapidFISH slide hybridizer oven. The RNA probe panel used for the SAHA project was the CosMx™ Human Universal Cell Characterization Panel (Bruker, 121500002), except for inflammatory bowel disease ileum samples, which were run using the

CosMx™ Human 6K Discovery Panel (Bruker, 121500041). On the following day, after removing the coverslip, slides were quickly rinsed in 2X SCC, washed twice for 25 min at 37°C in pre-warmed 50% 4X SSC/50% formamide (ThermoFisher, AM9342), and washed again in 2X SCC twice for 2 min. The slides were then incubated in the dark at RT for 15 min with a 1:40 dilution of DAPI (part of Bruker, 121500020) in blocking buffer (part of Bruker, 121500006). After a 5-min wash in 1XPBS, cell segmentation marker staining was performed using a cocktail of CD298/B2M, PanCK, CD45, and CD68 antibodies. The antibodies are conjugated to a readout domain that binds fluorophores on-instrument. Slides were incubated in the dark at RT for 1 h with the morphology staining marker mix, prepared using the CosMx™ Human Universal Cell Segmentation Kit, RNA (Bruker, 121500020) and the CosMx™ Human CD68 A La Carte Marker, RNA (Bruker, 121500022), at the dilutions specified in the Bruker manual. Slides were then washed three times in 1X PBS for 5 min and transferred to 2X SSC. For most samples, the protocol spanned three days, meaning that at this stage, the adhesive frame was removed, and slides were stored ON in 2X SSC at 4°C, protected from light. The only exceptions were stomach and lymph node samples, which were fully processed and loaded on the instrument in just two days. On the following day, the flow cells were assembled using the Flow Cell Assembly Tool provided by Bruker and Bruker glass coverslips with ports (CosMx™ Flow Cell Assembly Kit, Bruker, 122000061). They were then kept in 2X SSC, ensuring the solution filled the flow cells to prevent section dehydration, and stored in the dark until loading onto the CosMx instrument.

For the CosMx Protein assay, slides were baked for just 1 h at 65°C in a vertical position. Similar to the RNA assay, after baking slides were equilibrated for 3 min at RT and then immersed in CitriSolv twice for 5 minutes. In the case of the protein workflow, this was followed by a series of washes: two 10 min washes in 100% Et-OH, two 5 min washes in 95% EtOH, one 5 min wash in 70% EtOH, and two 5 min washes in 1XPBS. The target retrieval step was performed as described above for the RNA assay, with the only difference that after the 15 min retrieval, the solution containing the slides was left to cool at RT for 25 min. The slides were then transferred to 1XPBS and washed three times for 5 min. At this point, the incubation frame (part of Bruker 121500008) was applied to the slides. Sections were incubated with blocking Buffer W (part of Bruker 121500008) for 1 h at RT, followed by ON incubation at 4°C with a single mix containing both the morphology marker antibodies for segmentation (CosMx Human Universal Cell Segmentation Kit, IO PanCK/CD45 Supplemental Segmentation Kit, and CD3 A La Carte Marker, Bruker 121500026, 121500027, and 121500028) and the antibodies from the CosMx Human Immuno-oncology 64-plex panel (Bruker, 121500010). The sections were covered with a plastic coverslip (part of Bruker 121500008) during ON incubation. The following day, after removing the coverslip, the slides were washed three times for 10 min in 1XTBS-T (ThermoFisher, J77500.K2) and once for 2 min in 1XPBS. During the 1XTBS-T washes, fiducials were prepared as for the RNA assay. For the protein assay, the final fiducial working concentration was 0.00005%, requiring a two-step serial dilution in 1XTBS-T, as recommended by the manual. After a 5 min incubation at RT with fiducials, slides were washed once with 1XPBS for 5 min, fixed with 4% PFA (Electron Microscopy Sciences, 15710) for 15 min at RT in the dark, washed three times in 1XPBS for 5 min each, and incubated for 10 min at RT with a 1:40 dilution of DAPI (Bruker 121500026) in 1XPBS. The slides were then washed twice more in 1XPBS for 5 min, incubated with freshly prepared 100 mM NHS-Acetate for 15 min protected from light at RT, and subjected to a final 5 min wash in 1XPBS. As for the RNA assay, for most of the SAHA protein assays, the protocol extended over three days. Slides were transferred to fresh 1XPBS tubes and stored at 4°C in the dark ON. On the following day, flow cells were

assembled as described above, kept in 1XPBS in the dark, and loaded onto the CosMx instrument.

To set up a new CosMx runs on the Bruker CosMx Spatial Molecular Imager (SMI), the Bruker manual MAN-10161 was used as a guide. Different versions of the manual were followed throughout the SAHA project, and various SMI instrument software versions were installed on the machine over time. **Supplementary Table 2** lists the instrument manual and software versions for each analyzed sample. The SMI Control Center webpage interface allows for the setup of all run specifications, as well as the assignment of FOVs. The setup begins with configuring a new flow cell, the first step of which is defining the primary information for the run, including the Pre-Bleaching Profile and the Cell Segmentation Profile. As these profiles are tissue-type specific, they were selected based on Bruker's recommendations in MAN-10161, but they ultimately ended up being Pre-Bleaching Profile C and Cell Segmentation Profile A for all our runs, both RNA and protein. The probe panel and cell segmentation kits used also needed to be specified at this stage. The sensor-based interactive SMI Control Center interface guided the loading of the instrument. The Imaging Tray (CosMx RNA Imaging Tray, Bruker 122000156, 122000157, or 122000158, CosMx Protein Imaging Tray, Bruker 122000162 or 122000163), flow cells, and buffers required for the run (CosMx RNA Instrument Buffer Kit, Bruker 100480 or 100481, CosMx Protein Instrument Buffer Kit, Bruker 100482) were loaded into their designated slots. For RNA assays, RNase inhibitors (Bruker, 121500004) were added to a specific well of the Imaging Tray. For all runs, two enzymes - Catalase and Pyranose Oxidase (part of Bruker 100480, 100481, and 100482) - needed to be resuspended, centrifuged, and added free of precipitate to Buffer 4 in advance. Once the assembled flow cell were loaded onto the instrument and all run parameters were approved, the system proceeded through a deck validation step, an instrument preparation step, and a preliminary morphology marker scan to allow the FOVs placement. RNA target readout on the CosMx SMI instrument was performed as described in He et al. [41]. Reporter Wash, Imaging, and Strip Wash Buffers all supplied by Bruker Spatial Biology. At this point, the FOV Selection Workspace opened, and the FOV Placement Tool enabled for the placement, movement, or deletion of individual FOVs or grids of FOVs over the scanned image of the section. For large tissue areas, a serial H&E scan was used in advance by pathologists to annotate the image and define the regions of interest to be covered by the available FOVs. For TMAs, we aimed to allocate a predefined number of FOVs to individual tissue cores. Once the FOVs were reviewed and approved, the machine began cycling. RNA readout began by flowing 100 µl of Reporter Pool 1 into the flow cell and incubating for 15 min. Reporter Wash Buffer (1 mL) was flowed to wash unbound reporter probes, and Imaging Buffer was added to the flow cell for imaging. Eight Z-stack images (0.8 µm step size) for each FOV were acquired, and photocleavable linkers on the fluorophores of the reporter probes were released by UV illumination and washed with Strip Wash buffer. The fluidic and imaging procedure was repeated for all the reporter pools, and the different rounds of reporter hybridization (based on assay plex) imaging were repeated multiple times to increase target detection sensitivity. Cell morphology was imaged on-instrument prior to RNA or protein readout by adding fluorophore-bound reporters to the flow cell and capturing eight z-stack images in the channels 488 nm (CD298/B2M), 532 nm (PanCK), 594 nm (CD45), 647 nm (CD68), and 385 nm (DAPI). Runs lasted anywhere from two to ten days, depending on the panel type and plex, and the number of FOVs. CosMx data were automatically uploaded to Bruker's cloud-based AtoMx Spatial Analysis Platform both during and after the run.

Single-nuclei sequencing (snPATHO-seq)

Single nucleus RNA sequencing (snRNA-seq) was performed following the snPATHO-Seq protocol as previously described [42]. Two scrolls of 30–50 µm thickness were obtained from each FFPE sample, adjacent to the sections used for CosMx, Xenium, and H&E staining. Scrolls were collected into 1.5-mL Eppendorf tubes, stored at 4°C in Ziplock bags containing desiccants to control humidity, and processed within one week. For nuclei isolation, scrolls were dewaxed by three sequential washes in 1 mL of xylene (Millipore Sigma, 214736) for 10 minutes each, with the first xylene wash performed at 55°C to enhance paraffin removal. Rehydration was achieved through serial immersions in decreasing concentrations of ethanol (100% twice, followed by 70%, 50%, and 30%; each for 1 minute) (Millipore Sigma, E7023), followed by a single wash with 1 mL of RPMI 1640 medium (Gibco, 11875093).

Tissues were then digested in RPMI 1640 supplemented with 1 mg/mL Liberase TH (Millipore Sigma, 5401151001) and 1 U/µL RNase inhibitor (Thermo Fisher Scientific, EO0382). The scrolls were fragmented using a pellet pestle, and the digestion volume was adjusted to 1 mL. Digestion proceeded at 800 rpm in a Thermomixer. Following digestion, 400 µL of EZ Lysis Buffer (Sigma-Aldrich, NUC-101) was added, mixed, and centrifuged at 850 × g for 5 minutes at 4°C. The nuclei-containing pellet was resuspended in EZ Lysis Buffer with 2% BSA (Miltenyi, 130-091-376) and RNase inhibitor, then homogenized by pestle and pipetting. The suspension was filtered through a 70-µm strainer (pluriSelect, 43-10070-50) and centrifuged. The nuclei pellet was washed three times with 1× PBS containing 1% BSA (Gibco, 70011044), followed by two washes with 0.5× PBS containing 0.02% BSA. Final resuspension was performed in 500–1000 µL of 0.5× PBS with 0.02% BSA, depending on pellet size, and filtered through a 40-µm strainer (pluriSelect, 43-10040-50).

Nuclei were quantified using the Luna-FX7 instrument with Acridine Orange/Propidium Iodide staining (Logos). For immediate processing, nuclei suspensions were kept on wet ice. snRNA-seq libraries were prepared using the Chromium X Controller (10x Genomics) and the Chromium Fixed RNA Profiling Reagent Kits for multiplexed samples (Chromium Fixed RNA Kit, PN-1000475; Chromium Next GEM Chip Q, PN-1000418; Dual Index Kit TS Set A, PN-1000251), following the manufacturer's user guide (CG000527, Rev E). For cryopreservation, nuclei suspensions were supplemented with 10% glycerol and 0.1× Enhancer (10x Genomics, PN-2000482), rested on ice for 10 minutes, and stored at -80°C.

Hybridization was performed using 500,000–1.5 million nuclei per sample at 42°C for 20 hours. Barcoding reagents BC1–BC4 were used. Post-hybridization washes were conducted in a pooled setting according to the user guide with an additional wash step. Approximately 10,000 nuclei were targeted for capture per sample. An extra cycle was added during the pre-amplification PCR step, and indexing PCR was optimized to achieve final library concentrations between 50 and 200 nM. Library quality was assessed using a Fragment Analyzer 5200 (Agilent) and quantified using a Qubit Flex Fluorometer (Thermo Fisher Scientific). Libraries were sequenced on an Illumina NovaSeq 6000 using a 28 × 10 × 10 × 90 bp read configuration, targeting 20,000–30,000 read pairs per nucleus.

Transcript count matrices generated by Cell Ranger v8.0.0 (10x Genomics) were imported into Seurat v5.0.1 for downstream analysis [43–47]. Doublet identification was performed using scDblFinder v1.14.0 with a preset doublet rate of 10%, reflecting the expected frequency in Single Cell Gene Expression Flex multiplexing experiments [48]. Quality control based on UMI and gene count distributions identified a population of low-complexity droplets, which lacked

distinct transcriptomic signatures and were excluded from further analysis. Nuclei flagged as doublets or containing fewer than 1,000 detected genes were removed, ensuring retention of major cell populations as validated by comparison with the original dataset. Normalization and highly variable feature selection were conducted using SCTransform with default parameters. Dimensionality reduction was performed using principal component analysis (PCA), with the first 30 principal components guiding Uniform Manifold Approximation and Projection (UMAP) embedding (RunUMAP) and Louvain clustering.

Xenium Slide Preparation and In Situ Gene Expression Assay

Sections for Xenium assays were prepared according to the *Xenium In Situ for FFPE—Tissue Preparation Guide* (CG000578 Rev C, 10x Genomics) following the manufacturer's instructions. Briefly, 5-µm-thick FFPE tissue sections were floated in an RNase-free water bath and mounted onto the 10.45 mm × 22.45 mm sample area of Xenium slides (PN-3000941, 10x Genomics). Slides were air-dried at room temperature for 30 minutes, followed by a 3-hour incubation at 42°C on a Xenium Thermocycler Adapter plate positioned atop a 96-well thermal cycler (C1000 Touch, Bio-Rad) with the lid open. Slides were further dried ON at room temperature in the presence of desiccants.

Subsequent processing, including deparaffinization and decrosslinking, was performed following the *Xenium In Situ for FFPE—Deparaffinization and Decrosslinking Protocol* (CG000580 Rev C, 10x Genomics). Slides were incubated at 60°C for 2 hours, equilibrated at room temperature, then sequentially immersed in xylene (twice, 10 minutes each), 100% ethanol (twice, 3 minutes each), 96% ethanol (twice, 3 minutes each), 70% ethanol (once, 3 minutes), and water (once, 20 seconds). Following rehydration, slides were assembled into Xenium cassettes and hydrated with 1× PBS. Tissue sections were reverse crosslinked using a decrosslinking buffer containing tissue enhancer, urea, and perm enzyme B at 80°C for 30 minutes, followed by multiple PBS-T washes.

Slides were then processed according to the *Xenium In Situ Gene Expression User Guide* (CG000582 Rev E, 10x Genomics). Gene expression profiling was performed using the Xenium Human Multi-Tissue and Cancer Panel (10x-1000626), targeting 377 genes for prostate, ileum, appendix, pancreas, and colon samples, and the Xenium Human Breast Panel (10x-1000463,) targeting 380 genes for breast cancer samples. Probe hybridization involved probe denaturation at 95°C for 2 minutes, crash-cooling on ice, equilibration to room temperature, and 17-hour hybridization at 50°C. Post-hybridization, slides underwent standardized washes, ligation, amplification, autofluorescence quenching, and nuclear staining following the manufacturer's protocols.

Slides assembled into Xenium cassettes were processed using the Xenium Analyzer according to the *Xenium Analyzer User Guide* (CG000584 Rev D/E, 10x Genomics). Instrument setup included loading of the Xenium Decoding Consumables Kit (PN-1000487) with appropriate wash buffers and reagents. Slides were scanned to image fluorescently labeled nuclei, and fields of view (FOVs) were selected for sequencing. Data acquisition utilized the Xenium In Situ software suite (v1.9 for standard samples; v2.0 for multimodal segmentation samples), with simultaneous collection of gene expression and segmentation data for multimodal samples. Post-run, slides were washed with PBS-T and stored at 4°C in the dark until further staining and analysis.

RNAscope for quality assessment

Chromogenic in situ hybridization was performed on an automated stainer (Leica Bond RX, Leica Biosystems, Deer Park, IL) with RNAscope 2.5 LS Assay Reagent Kit-Red (Cat. # 322150, Advanced Cell Diagnostics, Newark, CA) and Bond Polymer Refine Red Detection (Cat. # DS9390, Leica Biosystems) following manufacturer's standard protocol. Positive control probe detecting a housekeeping gene (human PPIB, cat # 313908, Advanced Cell Diagnostics) and a negative control probe detecting bacterial (*Bacillus subtilis*) dapB gene (cat #312038, Advanced Cell Diagnostics) were used to assess RNA preservation and detection, and absence of non-specific signal, respectively. The chromogen was fast red and the counterstain hematoxylin. Positive RNA hybridization was identified as discrete, punctate chromogenic red dots under brightfield microscopy. Whole slide images were acquired with an Olympus VS200 slides scanner and VS200 ASW 4.1.1 software (Evident Scientific, Hamburg, Germany) using a 20X/0.80NA objective to generate whole slide images with a pixel size of 0.2738 µm. Image analysis was performed with QuPath 0.5.1 software (Bankhead, P. et al. QuPath: Open source software for digital pathology image analysis [49]. The positive cell detection and subcellular detection algorithms were used to detect cells and hybridization dots (individual spots and clusters), respectively. The mean number of estimated spots per cell was reported for each sample. The analysis we performed and validated by a board-certified veterinary pathologist (SM).

Data processing and annotation

For CosMx RNA and protein data, AtoMx Spatial Informatics Platform (SIP) was used for image processing and preprocessing of raw data. A slight modification was applied to the foundational pipeline available on the AtoMx platform (v1.3). For quality control, cells with the following cutoffs were flagged as low-quality cells: total transcript counts less than 20, negative probe counts more than 10%, count distribution 1, area outlier 0.01 (outlier p-value cutoff 0.01). FOV QC was done with default settings (mean, FOV count cutoff 100). The negative control probe quantile cutoff for target QC was set to 0.5, and detection was set to 0.01.

The datasets were normalized by scale factors and total counts, while 6k panels and combined datasets were normalized using total count normalization for scaling. For organ-specific analyses, count matrices were normalized using sc.pp.normalize_total() and log-transformed via sc.pp.log1p() (Scanpy v1.9.3). Dimensionality reduction was performed using PCA, followed by neighborhood graph construction (sc.pp.neighbors()) and UMAP embedding (sc.tl.umap()). UMAP was generated with the following parameters: 50 PCs for clustering, 40 number of neighbors, 0.01 minimum distance, 5 spread, Cosine distance metric, 0.25 data fraction. Spatial networks were calculated based on the distance (50 um), and neighborhoods based on the Jaccard cutoff of 0.099 and cosine distance. The datasets were exported for cell type annotation and further downstream analysis. For initial automated cell type annotation of RNA data, we used Insitutype [50] with organ-specific profile matrices derived from published single-cell and spatial transcriptomics datasets (available via the SAHA GitHub repository; see **Code Availability**). For protein data, cell phenotyping was performed using SCIMAP based on a marker-guided gating strategy. Manual refinement was applied as needed following

unsupervised clustering to improve resolution of rare or ambiguous populations. Various batches and organ types were integrated for analysis using Harmony [51].

Organ-specific analyses

To characterize lymphoid architecture in lymph nodes, we applied a multimodal spatial analysis workflow. Spatial niche detection was performed using spaVAE [52], a dependency-aware variational autoencoder model. Normalized lymph node datasets were input into spaVAE using default parameters over 50 iterations. The resulting niche clusters were compared to Leiden-based transcriptomic clusters for biological interpretability. Germinal centers (GCs) and peri-GC regions were manually segmented using an interactive workflow implemented with matplotlib.widgets.PolygonSelector and matplotlib.path.Path. Visualizations were generated in Jupyter notebooks using %matplotlib tk, enabling real-time polygon annotation of GC boundaries. Cells were classified based on spatial overlap as intra-GC, peri-GC, or non-GC. For spatial cell–cell interaction analysis, neighborhood graphs were constructed using Squidpy's sq.gr.spatial_neighbors() function. Cell–cell interaction matrices were generated with sq.gr.interaction_matrix(), leveraging Leiden-inferred annotations to quantify contact frequencies across annotated cell types within GCs and adjacent regions. Gene expression patterns were visualized using Seaborn's clustermap() to highlight transcriptional diversity among niche clusters. Spatial autocorrelation statistics were calculated using Moran's I (sq.gr.spatial_autocorr()), excluding the top 1% of expression outliers. Genes with the highest spatial variability were selected for downstream interpretation and figure display. To identify differentially expressed genes (DEGs) between intra-GC and peri-GC compartments, we applied Wilcoxon rank-sum tests (scipy.stats.ranksums()), followed by multiple hypothesis correction using the Benjamini–Hochberg procedure (statsmodels.stats.multitest.multipletests()). Genes with adjusted $p < 0.05$ and $|\log FC| > 0.5$ were considered significant. Volcano plots were generated to highlight key upregulated and downregulated genes across compartments.

Comparison and integration of CosMx Protein and RNA data

To annotate protein data, we used SCIMAP (v1.3.2), a gating-based hierarchical cell annotation tool which takes a workflow with cell types noted by their marker genes to conduct cell typing (**Extended Data Fig 7a**). Integration of CosMx RNA and protein data was performed using MaxFuse (version 0.02). a Python (version 3.8.20) package that uses co-embedding, data smoothing, and cell matching to integrate "weakly-linked" multi-modal omics data that have little overlapping features [10]. Broad and granular annotations from RNA samples are integrated into serial sectioned protein samples to generate protein cell type annotations. We generated cell type mapping to analogous RNA and protein regions to create visual comparisons. To conduct the concordance comparison between SCIMAP and Maxfuse annotations, we examined how cells called by one modality are called by the other by calculating adjusted rand index and mapping a matrix of cell counts for the cell types of both modalities as a heatmap.
For RNA-protein correlations and concordance comparisons, all analyses were conducted using R version 4.4.3 and the following R packages: Seurat (v5.2.1), reticulate (v1.41.0), anndata (v0.7.5.6), dplyr (v1.1.4), ggplot2 (v3.5.2), ggrepel (v0.9.6), reshape2 (v1.4.4), and RColorBrewer (v1.1.3). No cell-wise or feature-wise filtering was applied to either the transcriptomic or proteomic datasets for this analysis. We identified 53 features common to both

RNA and protein modalities across 15 matched tissue cross-sections from 9 different organs. For each tissue pair, the mean RNA and protein expression levels for each common feature were computed after excluding values equal to zero, to avoid bias from low-input measurements. Mean values were also calculated at the organ level by averaging feature expression across all tissue sections from the same organ. In addition, pooled averages were computed by aggregating all features across all organs. To assess the relationship between RNA and protein expression, we computed the log10-transformed mean expression values of each feature and visualized them using scatter plots, with log10(RNA mean) on the y-axis and log10(protein mean) on the x-axis. These plots were generated for tissue pairs, organs, and the aggregated dataset. Linear regression models were fit to each of these comparisons using the lm() function in base R, with the following formula: log10(RNA.mean) ~ log10(PRT.mean). We also generated analogous plots and regressions to compare average RNA and protein expression values across all common features within each tissue pair and organ. Spearman's rank correlation coefficient was used to calculate RNA-protein correlations across organs and genes.

Comparative analysis of H&E images with spatial transcriptomics datasets

Whole-slide H&E imaging data was processed using LazySlide [53]. Gastrointestinal tract samples (appendix, colon, ileum) were segmented and tesselated with tiles of 512 pixels at 0.5 µm/pixel (~20X magnification). For each slide, we randomly sampled 250 tiles and extracted high-dimensional morphological embeddings leveraging the CONCH multi-modal vision–language model [15]. Subsampling was performed to ensure equal contribution of various slides/tissue types. Tile embedding values were scaled, reduced with Principal Component Analysis (PCA) and visualized using the Isomap (scikit-learn) or Uniform Manifold Approximation and Projection (UMAP) algorithm [54] and clustered using the Leiden algorithm [55] at resolution 0.5 with Scanpy [56]. For downstream interpretation, we assembled a panel of 79 histolopathological terms related to instestinal biology or pathology. We computed the similarity between the text embedding of each term in each CONCH feature vector of each tile. Text embedding term values were compared between morphological clusters using a Wilcoxon test, and the top 3 most differential terms were used to describe each cluster.

In parallel, we applied CellViT [57] to the same whole-slide images to perform end-to-end nuclear segmentation and classification. Within each sampled tile, we quantified cell-type abundances (e.g., epithelial, immune, connective) and averaged these cellular proportions per morphological cluster previously derived by the CONCH features. To link tile-based morphological phenotypes with molecular cell-type composition, we performed canonical correlation analysis (CCA) implemented in scikit-learn between the relative abundance of each morphology cluster and the corresponding cell-type proportions inferred by the CosMx platform per tissue slide.

Integrative analysis of SAHA COL and CRC CosMx data

Downstream analysis was performed using Seurat (v5.0.1) [43–47] throughout to assess cell types and perform graph-based clustering. To harmonize gene probes across both datasets, gene probes targeting closely related genes (previously combined in an earlier spatial probe set but separated into individual genes in the current set) were merged. Specifically, genes originally

represented as single combined probes (e.g., *CCL3/L1/L3, CXCL1/2/3*) were merged into single meta-probes by summing their expression values across individual gene measurements. A complete list of merged genes is available in **Supplementary Table 3**. Genes without common representation across both spatial datasets were excluded to ensure consistent comparisons. After matching the probes, each FOV in the CRC sample was matched to an FOV from the COL sample to achieve relatively equal cell numbers (Figure 7, Extended Data Fig. 8).

Following this process, raw count matrices from each object were exported and combined using the merge() function from Seurat. Normalization, scaling, and PCA calculation were performed using standard Seurat functions. Objects were then integrated using Seurat's IntegrateLayers() function with the Harmony algorithm [51] (parameters: theta = 2, lambda = 0.1). After integration, Uniform Manifold Approximation and Projection (UMAP) embedding was performed using 30 principal components (PCs). Clusters were defined using a resolution of 0.3, and low-quality cells (Cluster 11) were excluded based on low feature counts. Prior to marker identification, the JoinLayers() function was applied as recommended by Seurat developers. Cluster markers were identified using Seurat's FindAllMarkers() function (parameters: min.pct = 0.2, logfc.threshold = 0.5, adjusted p-value < 0.05; Supplementary Table X).

Differentially expressed unique genes highlighted in Fig. 7c were identified with the FindMarkers() function using the MAST test (min.pct = 0.1, logfc.threshold = 0.5, adjusted p-value < 0.05; Supplementary Table X). Spatially differentially expressed genes (Fig. 7d-f) were computed using the Voyager tool [58] to calculate Moran's I. Field of views (FOVs) were clustered based on the top 200 spatially variable genes per field using principal component analysis (25 PCs), followed by k-means clustering (k = 2) as visualized in Fig. 7d.

Visualizations were generated with Seurat's functions: UMAPs (Fig 7a, Extended Data Fig. f,h) (DimPlot), Dotplots (Fig. 7h-2, Extended Data Fig. b,g) (DotPlot), violin plots (Fig 7c and e , Extended Data Fig. a) (VlnPlot), and pseudo-spatial images (Fig 7g-4, h-2, Extended Data Fig. h-1) (ImageDimPlot). Bar plots (Fig 7g-3, Extended Data Fig. c,f) were created using dittoBarPlot from dittoSeq [59], and spatial crypt visualizations were generated using ggplot2's geom_point() (Fig. 7b,f, Extended Data Fig. d,e). Cell-cell interaction analysis (Fig. 7h-3) was performed using CellChat software [60] (conversion factor = 0.18; interaction range = 250; scale.distance = 4.5; contact range = 20).

Data explorer generation

All generated data were made available for interactive exploration using Vitessce [61]. For each individual sample, cell segmentation polygons were converted into a JSON format in which each cell is represented as an object containing a list of [x, y] coordinate pairs corresponding to its boundary vertices. The visualization interface included a "Spatial" viewer, which displays the sample in physical (x, y) space, allowing users to explore gene expression for any gene alongside cell-level annotations derived from downstream analyses. Additional panels included a "Quality Control" window showing violin plots for metrics such as transcripts per cell and unique genes per cell, a "Features" window listing available genes, and a "Cell Labels" window summarizing cell annotations. All panels were linked, enabling dynamic cross-filtering: selections made in one viewer were automatically reflected across the others. Files generated for the Vitessce viewers are hosted on Zenodo and the script used to generate these files was deposited on github (See **Data and Code Availability**).

Data and Code Availability

Raw sequences, images, and processed datasets from single-nuclei sequencing and spatial transcriptomics are available via Zenodo (https://zenodo.org/communities/saha) and web portal (https://saha-project.org), and code blocks used to analyze the data can be accessed in the GitHub repository (available upon acceptance; https://github.com/saha-project).

Acknowledgments

We thank the WorldQuant, GI Research Foundation, Bumrungrad International Hospital, the National Institutes of Health (R01MH117406), and the LLS (MCL 7001-18, LLS 9238-16, 7029-23). E.A., Y.Z., and A.F.R received funding from Angelini Ventures S.p.A. Rome, Italy. P.S.D. thanks NIDDK (1U01DK134321, 5R01DK135620), NIAID (1U19AI181102), and Digestive Health Foundation for the support.

We would like to acknowledge former SAHA members from NanoString Technologies, whose contribution was crucial for establishing and generating the early phase of the project, specifically Nathan Schurman, Joachim Schmid, Raymond Tecotzky, Sarah Church, and Charlie Glaser. Most importantly, we thank the patients and their family members who provided valuable samples for this research.

Author contributions

Conceptualization: J.P., C.E.M., R.E.S., S.L.H., A.A., R.D.G., E.H.

Patient sample coordination: E.H., B.R., R.C., S.P., F.S.

Experiment and data generation: A.A., R.D.G., H.C., S.M., P.S.D., Y.L., L.P., K.Y., A.H., M.K., D.M., L.W., A.W., M.P., A.W., Y.L.

Investigation and data visualization: J.P., E.O., N.B., F.S.D., L.Z., M.M., Y.Z., E.A., J.K., M.R.A., E.M., J.R., Jac.P., A.A.A., P.D.,

Data management and portal development: J.P., T.N., M.M., F.S.D., Jac.P.

Supervision: C.E.M., R.E.S., S.L.H. A.F.R., J.T.P., L.M., O.E., G.C., M.L., J.B., Ja.K.

Writing: J.P., R.D.G., F.S.D., L.Z., Y.Z., A.F.R., E.A., A.A.A., E.O., N.B., J.T.P., C.E.M., S.B., S.R., P.D., S.M.L., A.B., T.N., C.E.M.

All authors discussed the results and contributed to the final manuscript.

Competing interests

C.E.M. serves on the Scientific Advisory Board of Cellanome Inc. Competing interests for G.C. is detailed here: https://arep.med.harvard.edu/gmc/tech.html. Ja.K. is co-founder and holds equity in iollo and ExactRx (Celeste Health, Inc) and is an advisor to Everfur (Strand Health, Inc) but declares no non-financial competing interests. E.M., S.R., P.D., J.R., Y.L., L.P., S.B., M.P., K.Y., A.H., M.K., D.M., L.W., A.W., and J.B. are current/previous NanoString Technologies or Bruker Spatial Biology employees.

SUPPLEMENTARY TABLES

Supplementary Table 1. SAHA Cohort Demographics and Clinical Metadata.
Summary of demographic and clinical characteristics of the SAHA cohort, including patient age, sex, tissue of origin, comorbidity (if applicable), and sample designation.

Supplementary Table 2. SAHA Experimental Run Metadata.
Detailed metadata for all SAHA spatial transcriptomics runs, including information such as slide/sample identifiers, tissue types, assay panels, staining protocols, quality metrics/statistics, platform used (e.g., CosMx, Xenium), and batch/run identifiers.

Supplementary Table 3. Additional Information related to CRC Analysis.
Additional files regarding the CRC and COL comparative analysis including list of probe substitutes, differential gene expression lists, cell marker lists, full result list of Moran's I results.

REFERENCES

1. Palla, G., Fischer, D. S., Regev, A. & Theis, F. J. Spatial components of molecular tissue biology. *Nat. Biotechnol.* **40**, 308–318 (2022).
2. Park, J. *et al.* Spatial omics technologies at multimodal and single cell/subcellular level. *Genome Biol.* **23**, 256 (2022).
3. Rood, J. E. *et al.* The Human Cell Atlas from a cell census to a unified foundation model. *Nature* **637**, 1065–1071 (2025).
4. Rozenblatt-Rosen, O. *et al.* The Human Tumor Atlas Network: Charting Tumor Transitions across Space and Time at Single-Cell Resolution. *Cell* **181**, 236–249 (2020).
5. Velten, B. & Stegle, O. Principles and challenges of modeling temporal and spatial omics data. *Nat. Methods* **20**, 1462–1474 (2023).
6. Cook, D. P. *et al.* A Comparative Analysis of Imaging-Based Spatial Transcriptomics Platforms. *BioRxiv* (2023) doi:10.1101/2023.12.13.571385.
7. Wilkinson, M. D. *et al.* The FAIR Guiding Principles for scientific data management and stewardship. *Sci. Data* **3**, 160018 (2016).
8. Liu, X. *et al.* Spatial multi-omics: deciphering technological landscape of integration of multi-omics and its applications. *J. Hematol. Oncol.* **17**, 72 (2024).
9. Yu, Y., Mai, Y., Zheng, Y. & Shi, L. Assessing and mitigating batch effects in large-scale omics studies. *Genome Biol.* **25**, 254 (2024).
10. Chen, S. *et al.* Integration of spatial and single-cell data across modalities with weak linkage. *BioRxiv* (2023) doi:10.1101/2023.01.12.523851.
11. Novoselsky, R. *et al.* Intracellular polarization of RNAs and proteins in the human small intestinal epithelium. *PLoS Biol.* **22**, e3002942 (2024).
12. Edfors, F. *et al.* Gene-specific correlation of RNA and protein levels in human cells and tissues. *Mol. Syst. Biol.* **12**, 883 (2016).
13. Sanchez de Groot, N. *et al.* RNA structure drives interaction with proteins. *Nat. Commun.*

10, 3246 (2019).

14. Liu, S. *et al.* The role of CD276 in cancers. *Front. Oncol.* **11**, 654684 (2021).
15. Lu, M. Y. *et al.* A visual-language foundation model for computational pathology. *Nat. Med.* **30**, 863–874 (2024).
16. Liu, Y. & Chen, Y.-G. Intestinal epithelial plasticity and regeneration via cell dedifferentiation. *Cell Regen (Lond)* **9**, 14 (2020).
17. Bala, P. *et al.* Aberrant cell state plasticity mediated by developmental reprogramming precedes colorectal cancer initiation. *Sci. Adv.* **9**, eadf0927 (2023).
18. Koltsova, E. K. & Grivennikov, S. I. IL-22 gets to the stem of colorectal cancer. *Immunity* **40**, 639–641 (2014).
19. Waldner, M. J., Foersch, S. & Neurath, M. F. Interleukin-6--a key regulator of colorectal cancer development. *Int. J. Biol. Sci.* **8**, 1248–1253 (2012).
20. Liu, X., Li, X., Wei, H., Liu, Y. & Li, N. Mast cells in colorectal cancer tumour progression, angiogenesis, and lymphangiogenesis. *Front. Immunol.* **14**, 1209056 (2023).
21. Conte, G. A. *et al.* S100 staining adds to the prognostic significance of the combination of perineural invasion and lymphovascular invasion in colorectal cancer. *Appl. Immunohistochem. Mol. Morphol.* **28**, 354–359 (2020).
22. Guo, J. A. *et al.* Pan-cancer Transcriptomic Predictors of Perineural Invasion Improve Occult Histopathologic Detection. *Clin. Cancer Res.* **27**, 2807–2815 (2021).
23. Wang, H. *et al.* Perineural invasion in colorectal cancer: mechanisms of action and clinical relevance. *Cell Oncol (Dordr)* **47**, 1–17 (2024).
24. Xue, M. *et al.* Schwann cells regulate tumor cells and cancer-associated fibroblasts in the pancreatic ductal adenocarcinoma microenvironment. *Nat. Commun.* **14**, 4600 (2023).
25. Zhang, B. *et al.* Single-cell RNA sequencing reveals intratumoral heterogeneity and potential mechanisms of malignant progression in prostate cancer with perineural invasion. *Front. Genet.* **13**, 1073232 (2022).

26. Zhang, Z. *et al.* Integrating clinical and genetic analysis of perineural invasion in head and neck squamous cell carcinoma. *Front. Oncol.* **9**, 434 (2019).
27. Liu, T. *et al.* Cancer-associated fibroblasts: an emerging target of anti-cancer immunotherapy. *J. Hematol. Oncol.* **12**, 86 (2019).
28. Sultana, P. & Novotny, J. Clusterin: a double-edged sword in cancer and neurological disorders. *EXCLI J.* **23**, 912–936 (2024).
29. Chen, H. *et al.* ANGPTL1 attenuates colorectal cancer metastasis by up-regulating microRNA-138. *J. Exp. Clin. Cancer Res.* **36**, 78 (2017).
30. Jiang, K. *et al.* Exosomal ANGPTL1 attenuates colorectal cancer liver metastasis by regulating Kupffer cell secretion pattern and impeding MMP9 induced vascular leakiness. *J. Exp. Clin. Cancer Res.* **40**, 21 (2021).
31. Chang, T.-Y., Lan, K.-C., Chiu, C.-Y., Sheu, M.-L. & Liu, S.-H. ANGPTL1 attenuates cancer migration, invasion, and stemness through regulating FOXO3a-mediated SOX2 expression in colorectal cancer. *Clin. Sci.* **136**, 657–673 (2022).
32. Tang, W. *et al.* LIF/LIFR oncogenic signaling is a novel therapeutic target in endometrial cancer. *Cell Death Discov.* **7**, 216 (2021).
33. Oliver, A. J. *et al.* Single-cell integration reveals metaplasia in inflammatory gut diseases. *Nature* **635**, 699–707 (2024).
34. Petukhov, V. *et al.* Cell segmentation in imaging-based spatial transcriptomics. *Nat. Biotechnol.* **40**, 345–354 (2022).
35. Si, Y. *et al.* FICTURE: scalable segmentation-free analysis of submicron-resolution spatial transcriptomics. *Nat. Methods* **21**, 1843–1854 (2024).
36. Zhang, J. *et al.* Tahoe-100M: A Giga-Scale Single-Cell Perturbation Atlas for Context-Dependent Gene Function and Cellular Modeling. *BioRxiv* (2025) doi:10.1101/2025.02.20.639398.
37. [2506.03373] A Foundation Model for Spatial Proteomics. https://arxiv.org/abs/2506.03373.

38. Wang, C. *et al.* scGPT-spatial: Continual Pretraining of Single-Cell Foundation Model for Spatial Transcriptomics. *BioRxiv* (2025) doi:10.1101/2025.02.05.636714.

39. Virshup, I., Rybakov, S., Theis, F. J., Angerer, P. & Wolf, F. A. anndata: Access and store annotated data matrices. *JOSS* **9**, 4371 (2024).

40. Allan, C. *et al.* OMERO: flexible, model-driven data management for experimental biology. *Nat. Methods* **9**, 245–253 (2012).

41. He, S. *et al.* High-Plex Multiomic Analysis in FFPE Tissue at Single-Cellular and Subcellular Resolution by Spatial Molecular Imaging. *BioRxiv* (2021) doi:10.1101/2021.11.03.467020.

42. Wang, T. *et al.* snPATHO-seq, a versatile FFPE single-nucleus RNA sequencing method to unlock pathology archives. *Commun. Biol.* **7**, 1340 (2024).

43. Butler, A., Hoffman, P., Smibert, P., Papalexi, E. & Satija, R. Integrating single-cell transcriptomic data across different conditions, technologies, and species. *Nat. Biotechnol.* **36**, 411–420 (2018).

44. Satija, R., Farrell, J. A., Gennert, D., Schier, A. F. & Regev, A. Spatial reconstruction of single-cell gene expression data. *Nat. Biotechnol.* **33**, 495–502 (2015).

45. Hao, Y. *et al.* Dictionary learning for integrative, multimodal and scalable single-cell analysis. *Nat. Biotechnol.* **42**, 293–304 (2024).

46. Stuart, T. *et al.* Comprehensive Integration of Single-Cell Data. *Cell* **177**, 1888-1902.e21 (2019).

47. Hao, Y. *et al.* Integrated analysis of multimodal single-cell data. *Cell* **184**, 3573-3587. (2021).

48. Germain, P.-L., Lun, A., Garcia Meixide, C., Macnair, W. & Robinson, M. D. Doublet identification in single-cell sequencing data using scDblFinder. *F1000Res.* **10**, 979 (2021).

49. Bankhead, P. *et al.* QuPath: Open source software for digital pathology image analysis. *Sci. Rep.* **7**, 16878 (2017).

50. Danaher, P. *et al.* Insitutype: likelihood-based cell typing for single cell spatial transcriptomics. *BioRxiv* (2022) doi:10.1101/2022.10.19.512902.
51. Korsunsky, I. *et al.* Fast, sensitive and accurate integration of single-cell data with Harmony. *Nat. Methods* **16**, 1289–1296 (2019).
52. Tian, T., Zhang, J., Lin, X., Wei, Z. & Hakonarson, H. Dependency-aware deep generative models for multitasking analysis of spatial omics data. *Nat. Methods* **21**, 1501–1513 (2024).
53. Zheng, Y., Abila, E., Chrenková, E., Winkler, J. & Rendeiro, A. F. LazySlide: accessible and interoperable whole slide image analysis. *BioRxiv* (2025) doi:10.1101/2025.05.28.656548.
54. McInnes, L., Healy, J. & Melville, J. UMAP: Uniform Manifold Approximation and Projection for Dimension Reduction. *arXiv* (2018) doi:10.48550/arxiv.1802.03426.
55. Traag, V. A., Waltman, L. & van Eck, N. J. From Louvain to Leiden: guaranteeing well-connected communities. *Sci. Rep.* **9**, 5233 (2019).
56. Wolf, F. A., Angerer, P. & Theis, F. J. SCANPY: large-scale single-cell gene expression data analysis. *Genome Biol.* **19**, 15 (2018).
57. Hörst, F. *et al.* CellViT: Vision Transformers for precise cell segmentation and classification. *Med. Image Anal.* **94**, 103143 (2024).
58. Moses, L. *et al.* Voyager: exploratory single-cell genomics data analysis with geospatial statistics. *BioRxiv* (2023) doi:10.1101/2023.07.20.549945.
59. Bunis, D. G., Andrews, J., Fragiadakis, G. K., Burt, T. D. & Sirota, M. dittoSeq: universal user-friendly single-cell and bulk RNA sequencing visualization toolkit. *Bioinformatics* **36**, 5535–5536 (2021).
60. Jin, S. *et al.* Inference and analysis of cell-cell communication using CellChat. *Nat. Commun.* **12**, 1088 (2021).
61. Keller, M. S. *et al.* Vitessce: integrative visualization of multimodal and spatially resolved single-cell data. *Nat. Methods* **22**, 63–67 (2025).

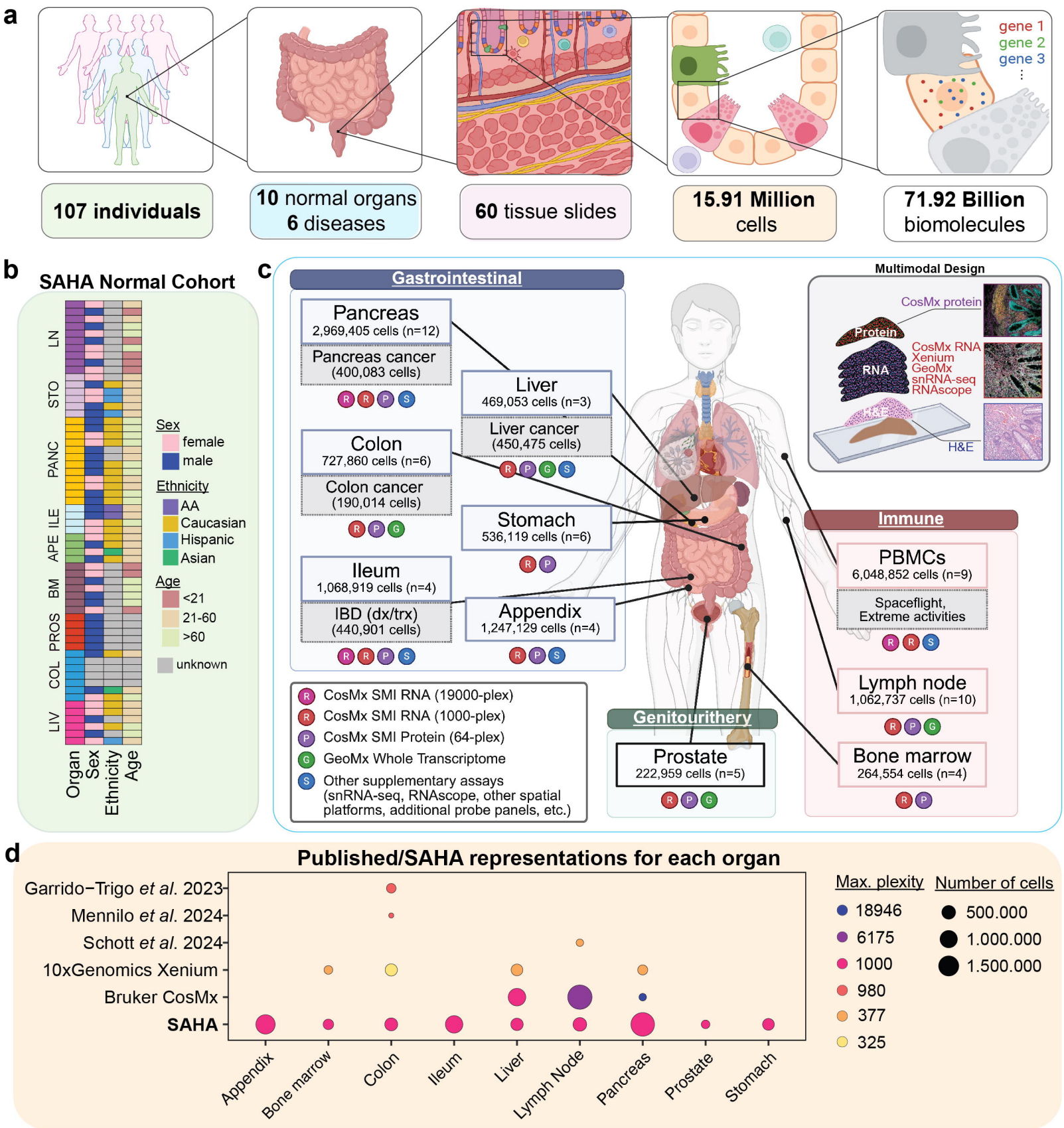
a
gene 1
gene 2
gene 3
107 individuals
10 normal organs
6 diseases
60 tissue slides
15.91 Million cells
71.92 Billion biomolecules
b
SAHA Normal Cohort
LN
STO
PANC
ILE
APE
BM
PROS
COL
LIV
Organ
Sex
Ethnicity
Age
Sex
female
male
Ethnicity
AA
Caucasian
Hispanic
Asian
Age
<21
21-60
>60
unknown
c
Gastrointestinal
Pancreas
2,969,405 cells (n=12)
Pancreas cancer
(400,083 cells)
Liver
469,053 cells (n=3)
Liver cancer
(450,475 cells)
Colon
727,860 cells (n=6)
Colon cancer
(190,014 cells)
Stomach
536,119 cells (n=6)
Ileum
1,068,919 cells (n=4)
IBD (dx/trx)
(440,901 cells)
Appendix
1,247,129 cells (n=4)
Multimodal Design
CosMx protein
Protein
RNA
CosMx RNA
Xenium
GeoMx
snRNA-seq
RNAscope
H&E
Immune
PBMCs
6,048,852 cells (n=9)
Spaceflight,
Extreme activities
Lymph node
1,062,737 cells (n=10)
Bone marrow
264,554 cells (n=4)
Genitourithery
Prostate
222,959 cells (n=5)
CosMx SMI RNA (19000-plex)
CosMx SMI RNA (1000-plex)
CosMx SMI Protein (64-plex)
GeoMx Whole Transcriptome
Other supplementary assays
(snRNA-seq, RNAscope, other spatial
platforms, additional probe panels, etc.)
d
Published/SAHA representations for each organ
Garrido−Trigo et al. 2023
Mennilo et al. 2024
Schott et al. 2024
10xGenomics Xenium
Bruker CosMx
SAHA
Appendix
Bone marrow
Colon
Ileum
Liver
Lymph Node
Pancreas
Prostate
Stomach
Max. plexity
18946
6175
1000
980
377
325
Number of cells
500.000
1.000.000
1.500.000

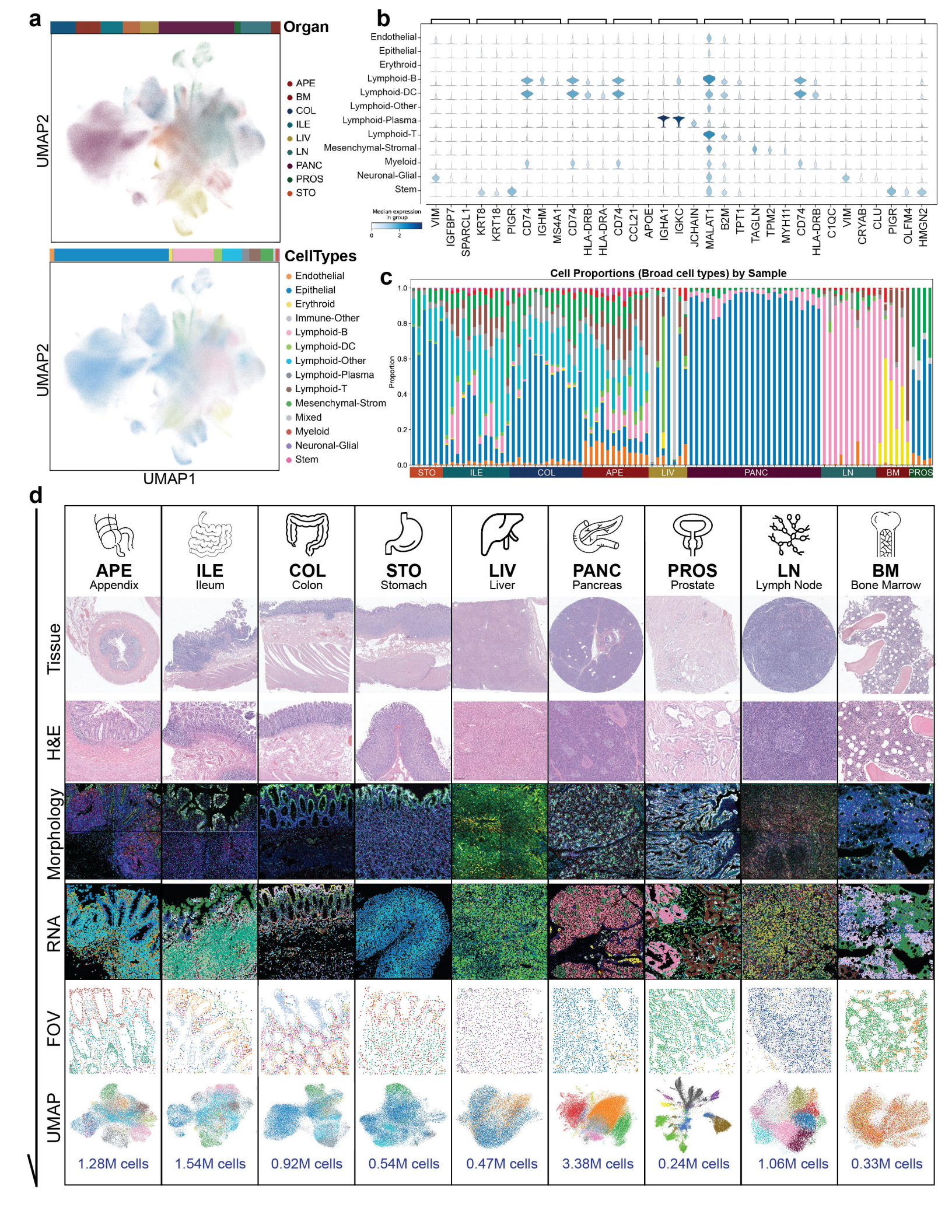
a
Organ
APE
BM
COL
ILE
LIV
LN
PANC
PROS
STO
UMAP2
CellTypes
Endothelial
Epithelial
Erythroid
Immune-Other
Lymphoid-B
Lymphoid-DC
Lymphoid-Other
Lymphoid-Plasma
Lymphoid-T
Mesenchymal-Strom
Mixed
Myeloid
Neuronal-Glial
Stem
UMAP1
b
Median expression in group
VIM
IGFBP7
SPARCL1
KRT8
KRT18
PIGR
CD74
IGHM
MS4A1
HLA-DRB
HLA-DRA
CCL21
APOE
IGHA1
IGKC
JCHAIN
MALAT1
B2M
TPT1
TAGLN
TPM2
MYH11
C1QC
CRYAB
CLU
OLFM4
HMGN2
c
Cell Proportions (Broad cell types) by Sample
Proportion
d
APE Appendix
ILE Ileum
COL Colon
STO Stomach
LIV Liver
PANC Pancreas
PROS Prostate
LN Lymph Node
BM Bone Marrow
Tissue
H&E
Morphology
RNA
FOV
UMAP
1.28M cells
1.54M cells
0.92M cells
0.54M cells
0.47M cells
3.38M cells
0.24M cells
1.06M cells
0.33M cells

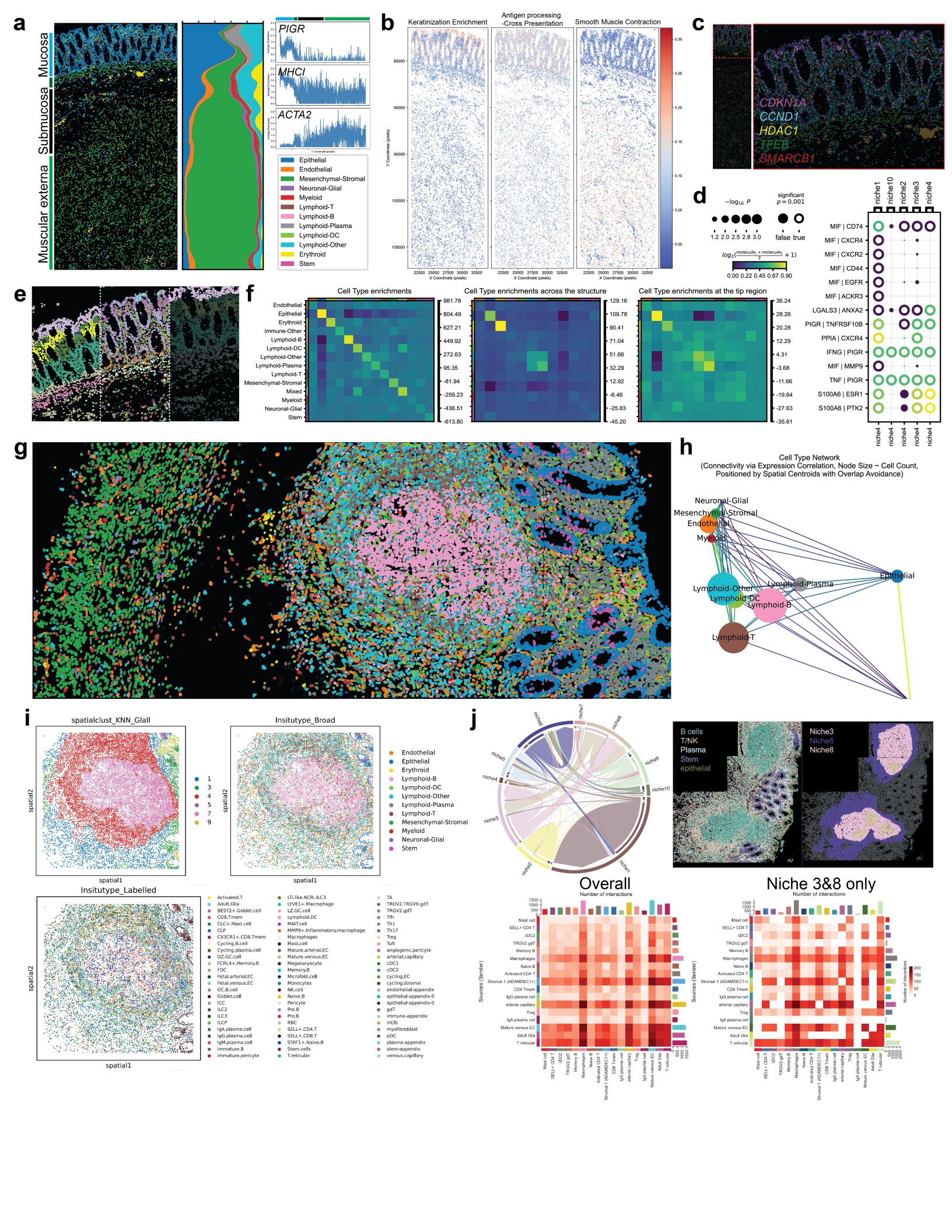
a
Mucosa
Submucosa
Muscular externa
PIGR
MHCI
ACTA2
Epithelial
Endothelial
Mesenchymal-Stromal
Neuronal-Glial
Myeloid
Lymphoid-T
Lymphoid-B
Lymphoid-Plasma
Lymphoid-DC
Lymphoid-Other
Erythroid
Stem
b
Keratinization Enrichment
Antigen processing -Cross Presentation
Smooth Muscle Contraction
Y Coordinate (pixels)
X Coordinate (pixels)
c
CDKN1A
CCND1
HDAC1
TFEB
SMARCB1
d
$-\log_{10} P$
significant $p = 0.001$
1.2 2.0 2.5 2.8 3.0
false true
$log_2(\frac{molecule_1 + molecule_2}{2} + 1)$
0.00 0.22 0.45 0.67 0.90
niche1
niche10
niche2
niche3
niche4
MIF | CD74
MIF | CXCR4
MIF | CXCR2
MIF | CD44
MIF | EGFR
MIF | ACKR3
LGALS3 | ANXA2
PIGR | TNFRSF10B
PPIA | CXCR4
IFNG | PIGR
MIF | MMP9
TNF | PIGR
S100A6 | ESR1
S100A6 | PTK2
e
f
Cell Type enrichments
Cell Type enrichments across the structure
Cell Type enrichments at the tip region
Endothelial
Epithelial
Erythroid
Immune-Other
Lymphoid-B
Lymphoid-DC
Lymphoid-Other
Lymphoid-Plasma
Lymphoid-T
Mesenchymal-Stromal
Mixed
Myeloid
Neuronal-Glial
Stem
981.78
804.49
627.21
449.92
272.63
95.35
-81.94
-259.23
-436.51
-613.80
129.16
109.78
90.41
71.04
51.66
32.29
12.92
-6.46
-25.83
-45.20
36.24
28.26
20.28
12.29
4.31
-3.68
-11.66
-19.64
-27.63
-35.61
g
h
Cell Type Network
(Connectivity via Expression Correlation, Node Size ~ Cell Count, Positioned by Spatial Centroids with Overlap Avoidance)
Neuronal-Glial
Mesenchymal-Stromal
Endothelial
Myeloid
Epithelial
Lymphoid-Other
Lymphoid-Plasma
Lymphoid-DC
Lymphoid-B
Lymphoid-T
i
spatialclust_KNN_GlaII
Insitutype_Broad
Insitutype_Labelled
spatial1
spatial2
1
3
4
5
7
9
Endothelial
Epithelial
Erythroid
Lymphoid-B
Lymphoid-DC
Lymphoid-Other
Lymphoid-Plasma
Lymphoid-T
Mesenchymal-Stromal
Myeloid
Neuronal-Glial
Stem
Activated.T
Adult.Glia
BEST2+.Goblet.cell
CD8.Tmem
CLC+.Mast.cell
CLP
CX3CR1+.CD8.Tmem
Cycling.B.cell
Cycling.plasma.cell
DZ.GC.cell
FCRL4+.Memory.B
FDC
Fetal.arterial.EC
Fetal.venous.EC
GC.B.cell
Goblet.cell
ICC
ILC2
ILC3
ILCP
IgA.plasma.cell
IgG.plasma.cell
IgM.plasma.cell
Immature.B
Immature.pericyte
LTi.like.NCR-.ILC3
LYVE1+.Macrophage
LZ.GC.cell
Lymphoid.DC
MAIT.cell
MMP9+.Inflammatory.macrophage
Macrophages
Mast.cell
Mature.arterial.EC
Mature.venous.EC
Megakaryocyte
Memory.B
Microfold.cell
Monocytes
NK.cell
Naive.B
Pericyte
Pre.B
Pro.B
RBC
SELL+.CD4.T
SELL+.CD8.T
STAT1+.Naive.B
Stem.cells
T.reticular
TA
TRDV2.TRGV9.gdT
TRGV2.gdT
Tfh
Th1
Th17
Treg
Tuft
angiogenic.pericyte
arterial.capillary
cDC1
cDC2
cycling.EC
cycling.stromal
endothelial-appendix
epithelial-appendix-0
epithelial-appendix-0
gdT
immune-appendix
mL3b
myofibroblast
pDC
plasma-appendix
stem-appendix
venous.capillary
j
niche1
niche2
niche3
niche4
niche5
niche6
niche7
niche8
niche9
niche10
B cells
T/NK
Plasma
Stem
epithelial
Niche3
Niche6
Niche8
Overall
Niche 3&8 only
Number of interactions
Sources (Sender)
Mast cell
SELL+ CD4 T
cDC2
TRGV2 gdT
Memory B
Macrophages
Naive B
Activated CD4 T
Stromal 1 (ADAMDEC1+)
CD8 Tmem
IgG plasma cell
arterial capillary
Treg
IgA plasma cell
Mature venous EC
Adult Glia
T reticular

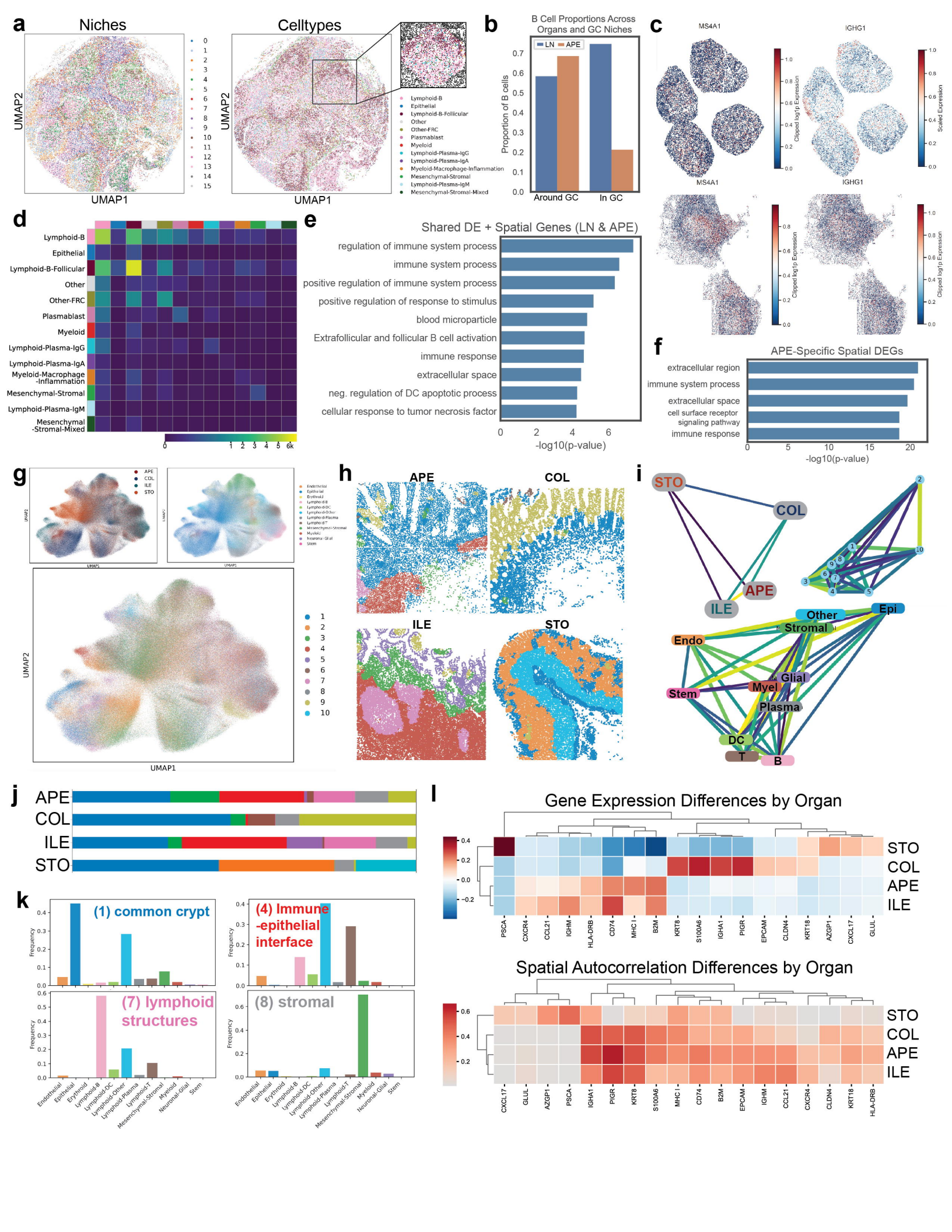
a
Niches
Celltypes
UMAP1
UMAP2
Lymphoid-B
Epithelial
Lymphoid-B-Follicular
Other
Other-FRC
Plasmablast
Myeloid
Lymphoid-Plasma-IgG
Lymphoid-Plasma-IgA
Myeloid-Macrophage-Inflammation
Mesenchymal-Stromal
Lymphoid-Plasma-IgM
Mesenchymal-Stromal-Mixed
b
B Cell Proportions Across Organs and GC Niches
LN
APE
Proportion of B cells
Around GC
In GC
c
MS4A1
IGHG1
Clipped log1p Expression
Scaled Expression
d
e
Shared DE + Spatial Genes (LN & APE)
regulation of immune system process
immune system process
positive regulation of immune system process
positive regulation of response to stimulus
blood microparticle
Extrafollicular and follicular B cell activation
immune response
extracellular space
neg. regulation of DC apoptotic process
cellular response to tumor necrosis factor
-log10(p-value)
f
APE-Specific Spatial DEGs
extracellular region
immune system process
extracellular space
cell surface receptor signaling pathway
immune response
-log10(p-value)
g
APE
COL
ILE
STO
UMAP1
UMAP2
h
APE
COL
ILE
STO
i
STO
COL
APE
ILE
Other
Epi
Stromal
Endo
Glial
Stem
Myel
Plasma
DC
T
B
j
APE
COL
ILE
STO
k
(1) common crypt
(4) Immune -epithelial interface
(7) lymphoid structures
(8) stromal
Frequency
Endothelial
Epithelial
Erythroid
Lymphoid-B
Lymphoid-DC
Lymphoid-Other
Lymphoid-Plasma
Lymphoid-T
Mesenchymal-Stromal
Myeloid
Neuronal-Glial
Stem
l
Gene Expression Differences by Organ
STO
COL
APE
ILE
PSCA
CXCR4
CCL21
IGHM
HLA-DRB
CD74
MHC I
B2M
KRT8
S100A6
IGHA1
PIGR
EPCAM
CLDN4
KRT18
AZGP1
CXCL17
GLUL
Spatial Autocorrelation Differences by Organ
STO
COL
APE
ILE
CXCL17
GLUL
AZGP1
PSCA
IGHA1
PIGR
KRT8
S100A6
MHC I
CD74
B2M
EPCAM
IGHM
CCL21
CXCR4
CLDN4
KRT18
HLA-DRB

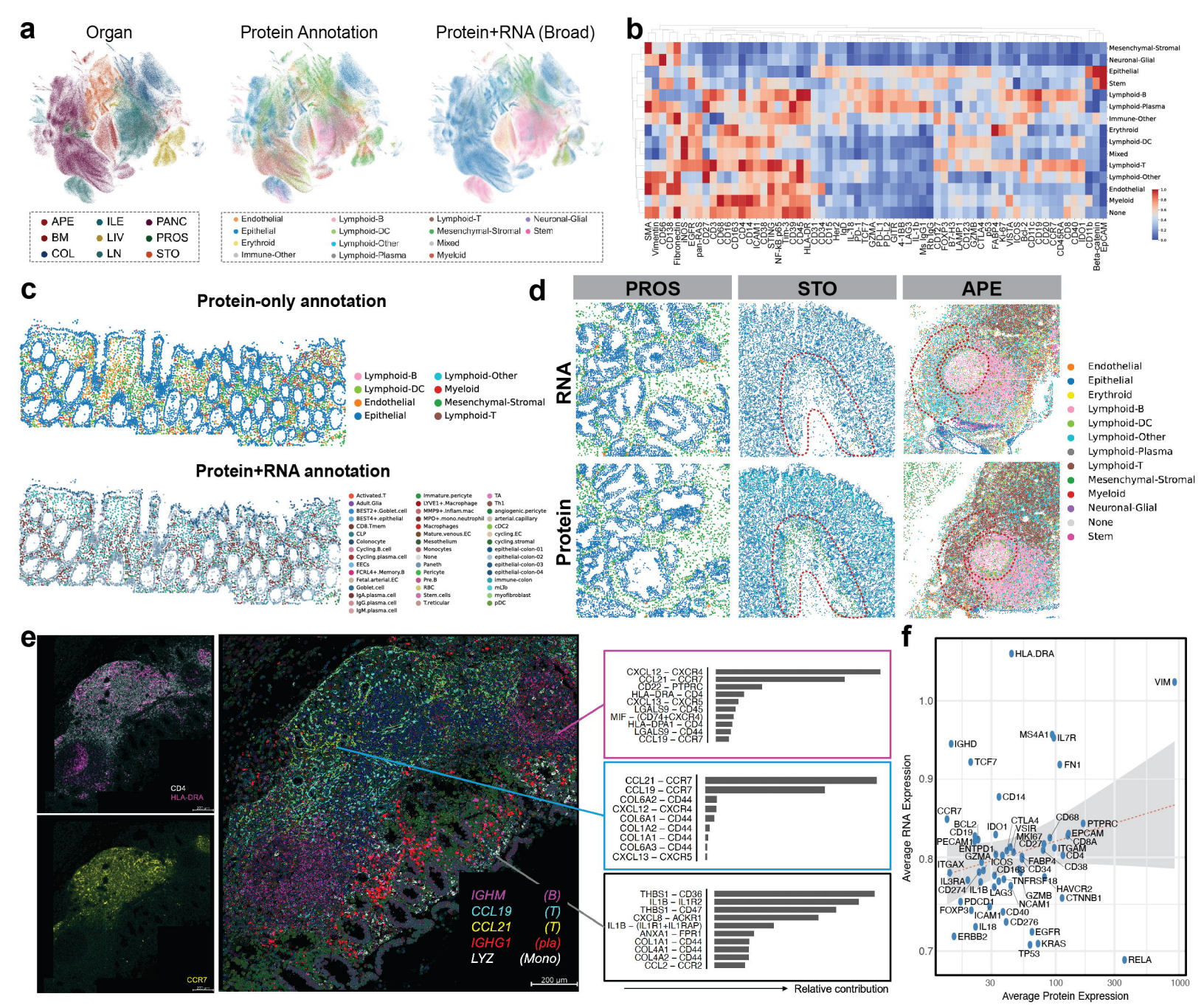

a
Organ
Protein Annotation
Protein+RNA (Broad)
APE
ILE
PANC
BM
LIV
PROS
COL
LN
STO
Endothelial
Epithelial
Erythroid
Immune-Other
Lymphoid-B
Lymphoid-DC
Lymphoid-Other
Lymphoid-Plasma
Lymphoid-T
Mesenchymal-Stromal
Mixed
Myeloid
Neuronal-Glial
Stem
b
Mesenchymal-Stromal
Neuronal-Glial
Epithelial
Stem
Lymphoid-B
Lymphoid-Plasma
Immune-Other
Erythroid
Lymphoid-DC
Mixed
Lymphoid-T
Lymphoid-Other
Endothelial
Myeloid
None
c
Protein-only annotation
Lymphoid-B
Lymphoid-DC
Endothelial
Epithelial
Lymphoid-Other
Myeloid
Mesenchymal-Stromal
Lymphoid-T
Protein+RNA annotation
d
PROS
STO
APE
RNA
Protein
Endothelial
Epithelial
Erythroid
Lymphoid-B
Lymphoid-DC
Lymphoid-Other
Lymphoid-Plasma
Lymphoid-T
Mesenchymal-Stromal
Myeloid
Neuronal-Glial
None
Stem
e
CD4
HLA-DRA
CCR7
IGHM (B)
CCL19 (T)
CCL21 (T)
IGHG1 (pla)
LYZ (Mono)
200 µm
CXCL12 – CXCR4
CCL21 – CCR7
CD22 – PTPRC
HLA–DRA – CD4
CXCL13 – CXCR5
LGALS9 – CD45
MIF – (CD74+CXCR4)
HLA–DPA1 – CD4
LGALS9 – CD44
CCL19 – CCR7
CCL21 – CCR7
CCL19 – CCR7
COL6A2 – CD44
CXCL12 – CXCR4
COL6A1 – CD44
COL1A2 – CD44
COL1A1 – CD44
COL6A3 – CD44
CXCL13 – CXCR5
THBS1 – CD36
IL1B – IL1R2
THBS1 – CD47
CXCL8 – ACKR1
IL1B – (IL1R1+IL1RAP)
ANXA1 – FPR1
COL1A1 – CD44
COL4A1 – CD44
COL4A2 – CD44
CCL2 – CCR2
Relative contribution
f
Average RNA Expression
Average Protein Expression
HLA.DRA
VIM
MS4A1
IL7R
IGHD
TCF7
FN1
CD14
CCR7
BCL2
CD19
IDO1
CTLA4
VSIR
MKI67
CD27
CD68
PTPRC
EPCAM
CD8A
PECAM1
ENTPD1
GZMA
ITGAM
CD4
ITGAX
ICOS
FABP4
CD38
CD163
CD34
IL3RA
CD274
IL1B
LAG3
TNFRSF18
HAVCR2
GZMB
CTNNB1
NCAM1
PDCD1
FOXP3
ICAM1
CD40
CD276
IL18
EGFR
ERBB2
KRAS
TP53
RELA

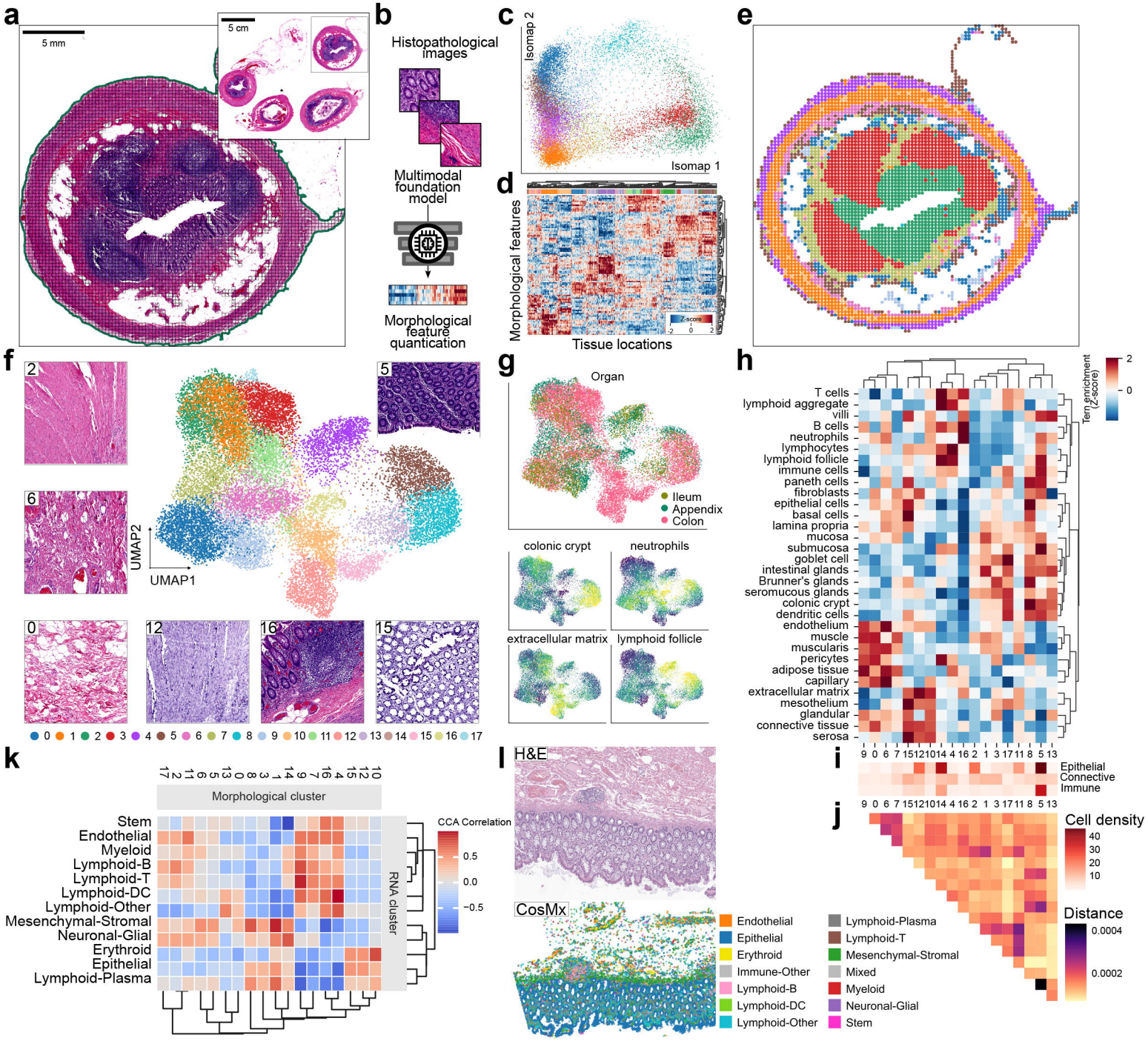
a
5 mm
5 cm
b
Histopathological images
Multimodal foundation model
Morphological feature quantication
c
Isomap 2
Isomap 1
d
Morphological features
Z-score
Tissue locations
e
f
2
5
6
UMAP2
UMAP1
0
12
16
15
0 1 2 3 4 5 6 7 8 9 10 11 12 13 14 15 16 17
g
Organ
Ileum
Appendix
Colon
colonic crypt
neutrophils
extracellular matrix
lymphoid follicle
h
Term enrichment (Z-score)
T cells
lymphoid aggregate
villi
B cells
neutrophils
lymphocytes
lymphoid follicle
immune cells
paneth cells
fibroblasts
epithelial cells
basal cells
lamina propria
mucosa
submucosa
goblet cell
intestinal glands
Brunner's glands
seromucous glands
colonic crypt
dendritic cells
endothelium
muscle
muscularis
pericytes
adipose tissue
capillary
extracellular matrix
mesothelium
glandular
connective tissue
serosa
9 0 6 7 15 12 10 14 4 16 2 1 3 17 11 8 5 13
i
Epithelial
Connective
Immune
j
Cell density
Distance
k
Morphological cluster
RNA cluster
CCA Correlation
Stem
Endothelial
Myeloid
Lymphoid-B
Lymphoid-T
Lymphoid-DC
Lymphoid-Other
Mesenchymal-Stromal
Neuronal-Glial
Erythroid
Epithelial
Lymphoid-Plasma
l
H&E
CosMx
Endothelial
Epithelial
Erythroid
Immune-Other
Lymphoid-B
Lymphoid-DC
Lymphoid-Other
Lymphoid-Plasma
Lymphoid-T
Mesenchymal-Stromal
Mixed
Myeloid
Neuronal-Glial
Stem

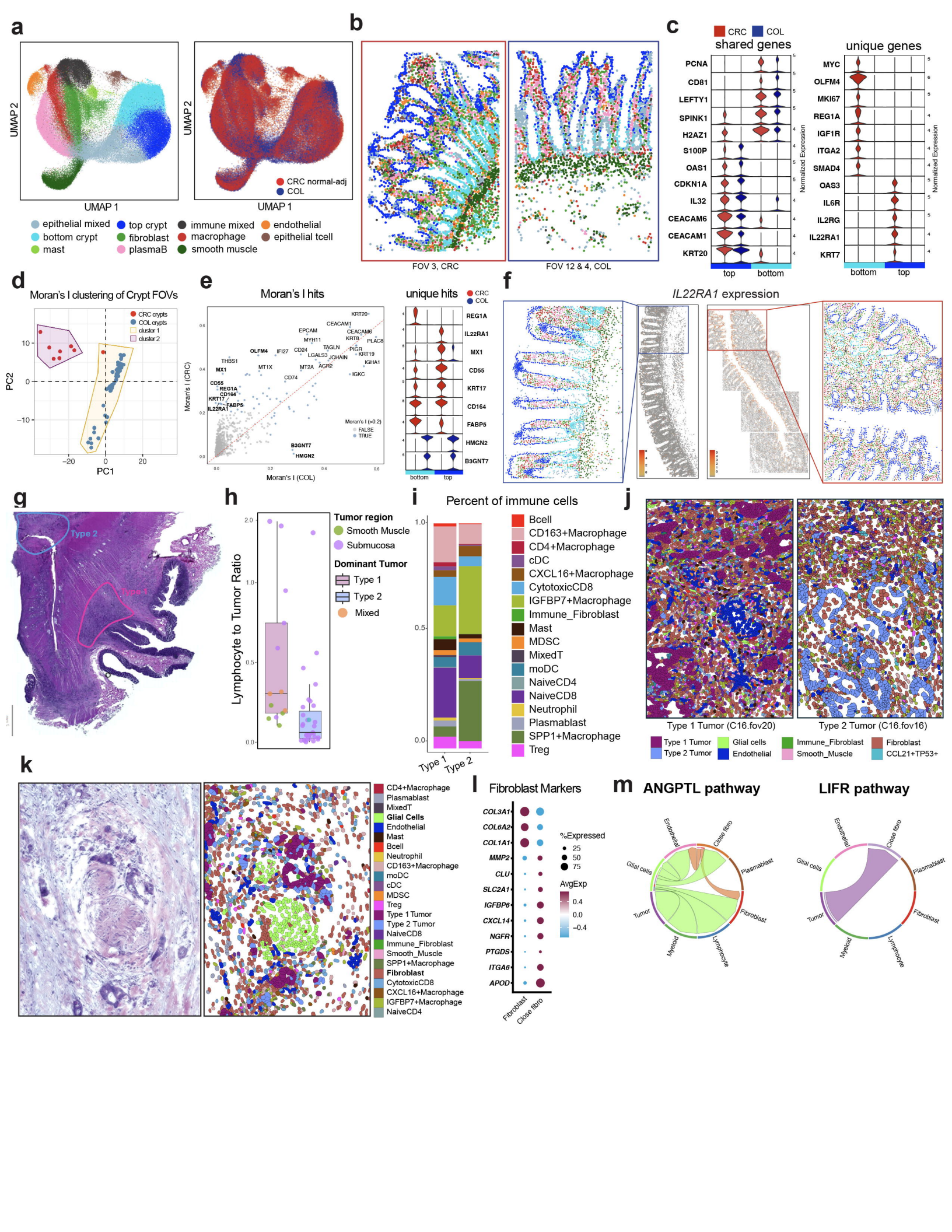
a
UMAP 2
UMAP 1
CRC normal-adj
COL
epithelial mixed
bottom crypt
mast
top crypt
fibroblast
plasmaB
immune mixed
macrophage
smooth muscle
endothelial
epithelial tcell
b
FOV 3, CRC
FOV 12 & 4, COL
c
CRC
COL
shared genes
unique genes
PCNA
CD81
LEFTY1
SPINK1
H2AZ1
S100P
OAS1
CDKN1A
IL32
CEACAM6
CEACAM1
KRT20
MYC
OLFM4
MKI67
REG1A
IGF1R
ITGA2
SMAD4
OAS3
IL6R
IL2RG
IL22RA1
KRT7
Normalized Expression
top
bottom
d
Moran's I clustering of Crypt FOVs
CRC crypts
COL crypts
cluster 1
cluster 2
PC1
PC2
e
Moran's I hits
Moran's I (CRC)
Moran's I (COL)
unique hits
CRC
COL
REG1A
IL22RA1
MX1
CD55
KRT17
CD164
FABP5
HMGN2
B3GNT7
bottom
top
f
IL22RA1 expression
g
Type 2
Type 1
h
Lymphocyte to Tumor Ratio
Tumor region
Smooth Muscle
Submucosa
Dominant Tumor
Type 1
Type 2
Mixed
i
Percent of immune cells
Type 1
Type 2
Bcell
CD163+Macrophage
CD4+Macrophage
cDC
CXCL16+Macrophage
CytotoxicCD8
IGFBP7+Macrophage
Immune_Fibroblast
Mast
MDSC
MixedT
moDC
NaiveCD4
NaiveCD8
Neutrophil
Plasmablast
SPP1+Macrophage
Treg
j
Type 1 Tumor (C16.fov20)
Type 2 Tumor (C16.fov16)
Type 1 Tumor
Type 2 Tumor
Glial cells
Endothelial
Immune_Fibroblast
Smooth_Muscle
Fibroblast
CCL21+TP53+
k
CD4+Macrophage
Plasmablast
MixedT
Glial Cells
Endothelial
Mast
Bcell
Neutrophil
CD163+Macrophage
moDC
cDC
MDSC
Treg
Type 1 Tumor
Type 2 Tumor
NaiveCD8
Immune_Fibroblast
Smooth_Muscle
SPP1+Macrophage
Fibroblast
CytotoxicCD8
CXCL16+Macrophage
IGFBP7+Macrophage
NaiveCD4
l
Fibroblast Markers
COL3A1
COL6A2
COL1A1
MMP2
CLU
SLC2A1
IGFBP6
CXCL14
NGFR
PTGDS
ITGA6
APOD
%Expressed
25
50
75
AvgExp
0.4
0.0
−0.4
Fibroblast
Close fibro
m
ANGPTL pathway
LIFR pathway
Endothelial
Close fibro
Plasmablast
Fibroblast
Lymphocyte
Myeloid
Tumor
Glial cells

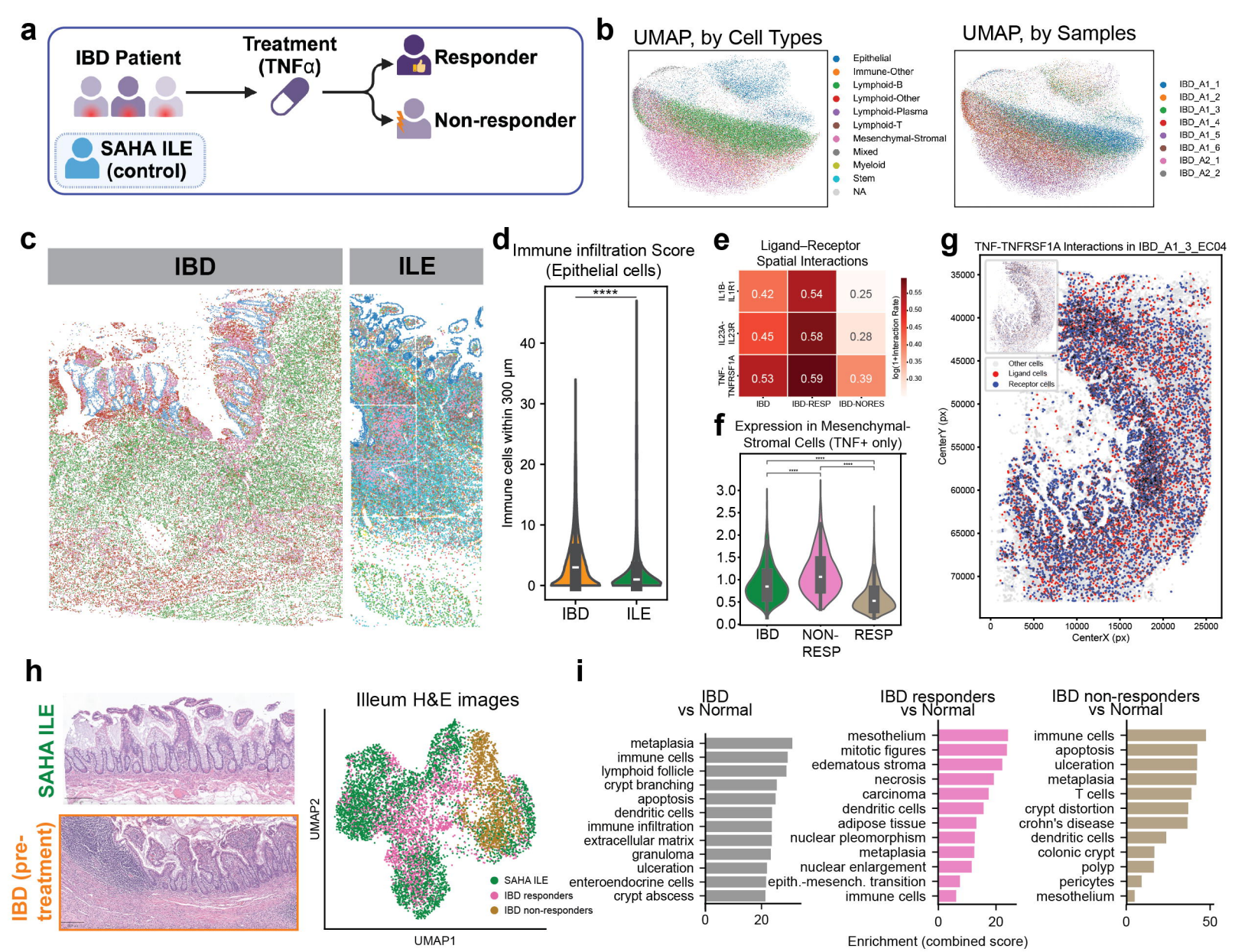
a
IBD Patient
Treatment (TNFα)
Responder
Non-responder
SAHA ILE (control)
b
UMAP, by Cell Types
Epithelial
Immune-Other
Lymphoid-B
Lymphoid-Other
Lymphoid-Plasma
Lymphoid-T
Mesenchymal-Stromal
Mixed
Myeloid
Stem
NA
UMAP, by Samples
IBD_A1_1
IBD_A1_2
IBD_A1_3
IBD_A1_4
IBD_A1_5
IBD_A1_6
IBD_A2_1
IBD_A2_2
c
IBD
ILE
d
Immune infiltration Score (Epithelial cells)
Immune cells within 300 µm
****
IBD
ILE
e
Ligand–Receptor Spatial Interactions
IL1B-IL1R1
IL23A-IL23R
TNF-TNFRSF1A
IBD
IBD-RESP
IBD-NORES
log(1+Interaction Rate)
f
Expression in Mesenchymal-Stromal Cells (TNF+ only)
IBD
NON-RESP
RESP
g
TNF-TNFRSF1A Interactions in IBD_A1_3_EC04
Other cells
Ligand cells
Receptor cells
CenterY (px)
CenterX (px)
h
SAHA ILE
IBD (pre-treatment)
Illeum H&E images
UMAP2
UMAP1
SAHA ILE
IBD responders
IBD non-responders
i
IBD vs Normal
metaplasia
immune cells
lymphoid follicle
crypt branching
apoptosis
dendritic cells
immune infiltration
extracellular matrix
granuloma
ulceration
enteroendocrine cells
crypt abscess
IBD responders vs Normal
mesothelium
mitotic figures
edematous stroma
necrosis
carcinoma
dendritic cells
adipose tissue
nuclear pleomorphism
metaplasia
nuclear enlargement
epith.-mesench. transition
immune cells
IBD non-responders vs Normal
immune cells
apoptosis
ulceration
metaplasia
T cells
crypt distortion
crohn's disease
dendritic cells
colonic crypt
polyp
pericytes
mesothelium
Enrichment (combined score)

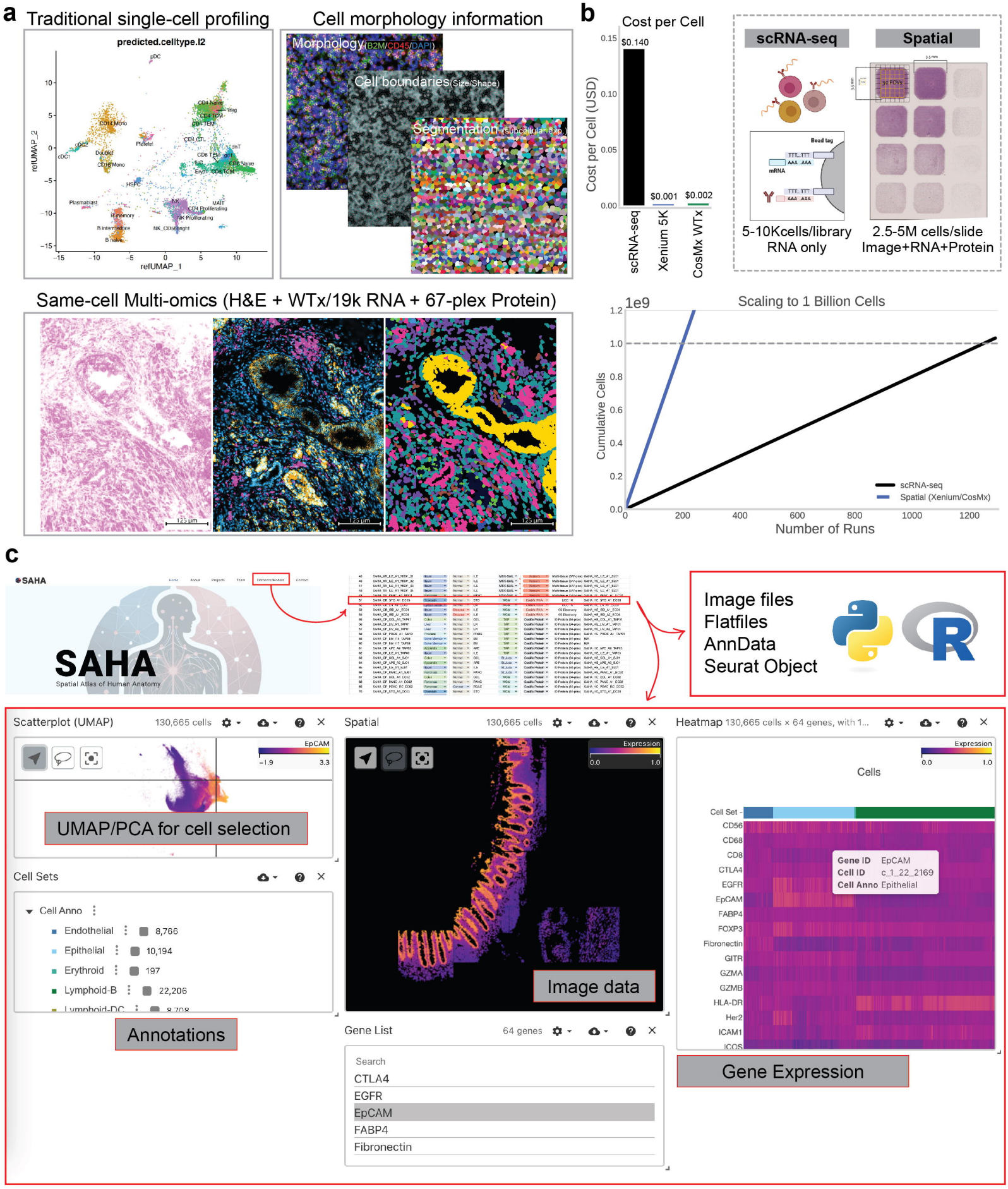
a
Traditional single-cell profiling
predicted.celltype.l2
refUMAP_1
refUMAP_2
Cell morphology information
Morphology (B2M/CD45/DAPI)
Cell boundaries (Size/Shape)
Segmentation (Subcellular exp.)
b
Cost per Cell
Cost per Cell (USD)
$0.140
$0.001
$0.002
scRNA-seq
Xenium 5K
CosMx WTx
scRNA-seq
Spatial
Bead tag
mRNA
5-10Kcells/library
RNA only
2.5-5M cells/slide
Image+RNA+Protein
Same-cell Multi-omics (H&E + WTx/19k RNA + 67-plex Protein)
125 µm
Scaling to 1 Billion Cells
1e9
Cumulative Cells
Number of Runs
scRNA-seq
Spatial (Xenium/CosMx)
c
SAHA
Spatial Atlas of Human Anatomy
Image files
Flatfiles
AnnData
Seurat Object
Scatterplot (UMAP)
130,665 cells
EpCAM
UMAP/PCA for cell selection
Cell Sets
Cell Anno
Endothelial 8,766
Epithelial 10,194
Erythroid 197
Lymphoid-B 22,206
Annotations
Spatial
130,665 cells
Expression
Image data
Gene List
64 genes
Search
CTLA4
EGFR
EpCAM
FABP4
Fibronectin
Heatmap 130,665 cells × 64 genes, with 1...
Cells
Cell Set
CD56
CD68
CD8
CTLA4
EGFR
EpCAM
FABP4
FOXP3
Fibronectin
GITR
GZMA
GZMB
HLA-DR
Her2
ICAM1
ICOS
Gene ID EpCAM
Cell ID c_1_22_2169
Cell Anno Epithelial
Gene Expression

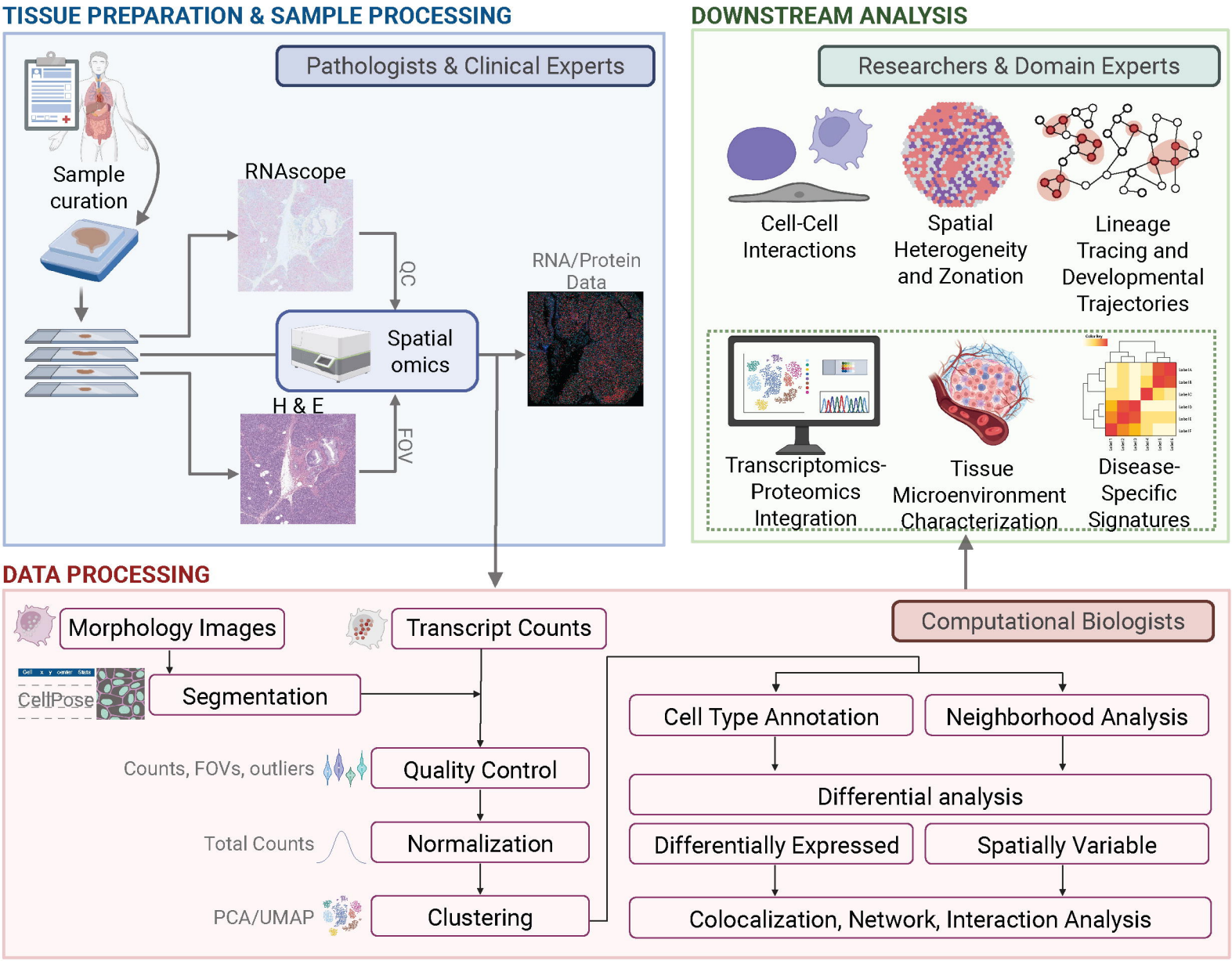
TISSUE PREPARATION & SAMPLE PROCESSING
Pathologists & Clinical Experts
Sample curation
RNAscope
QC
RNA/Protein Data
Spatial omics
H & E
FOV
DOWNSTREAM ANALYSIS
Researchers & Domain Experts
Cell-Cell Interactions
Spatial Heterogeneity and Zonation
Lineage Tracing and Developmental Trajectories
Transcriptomics-Proteomics Integration
Tissue Microenvironment Characterization
Disease-Specific Signatures
DATA PROCESSING
Computational Biologists
Morphology Images
Transcript Counts
CellPose
Segmentation
Counts, FOVs, outliers
Quality Control
Total Counts
Normalization
PCA/UMAP
Clustering
Cell Type Annotation
Neighborhood Analysis
Differential analysis
Differentially Expressed
Spatially Variable
Colocalization, Network, Interaction Analysis

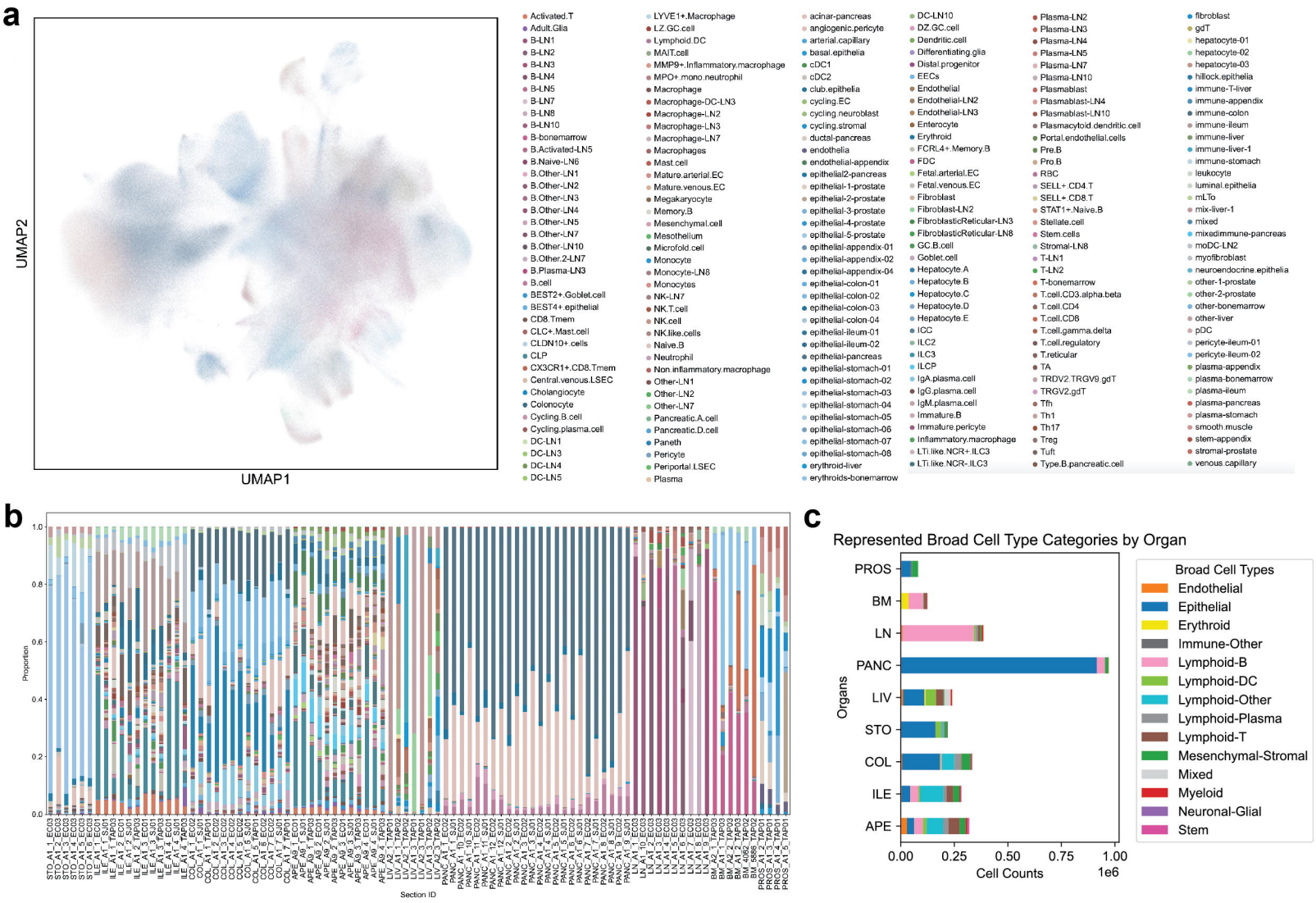
a
UMAP2
UMAP1
Activated.T
Adult.Glia
B-LN1
B-LN2
B-LN3
B-LN4
B-LN5
B-LN7
B-LN8
B-LN10
B-bonemarrow
B.Activated-LN5
B.Naive-LN6
B.Other-LN1
B.Other-LN2
B.Other-LN3
B.Other-LN4
B.Other-LN5
B.Other-LN7
B.Other-LN10
B.Other.2-LN7
B.Plasma-LN3
B.cell
BEST2+.Goblet.cell
BEST4+.epithelial
CD8.Tmem
CLC+.Mast.cell
CLDN10+.cells
CLP
CX3CR1+.CD8.Tmem
Central.venous.LSEC
Cholangiocyte
Colonocyte
Cycling.B.cell
Cycling.plasma.cell
DC-LN1
DC-LN3
DC-LN4
DC-LN5
LYVE1+.Macrophage
LZ.GC.cell
Lymphoid.DC
MAIT.cell
MMP9+.Inflammatory.macrophage
MPO+.mono.neutrophil
Macrophage
Macrophage-DC-LN3
Macrophage-LN2
Macrophage-LN3
Macrophage-LN7
Macrophages
Mast.cell
Mature.arterial.EC
Mature.venous.EC
Megakaryocyte
Memory.B
Mesenchymal.cell
Mesothelium
Microfold.cell
Monocyte
Monocyte-LN8
Monocytes
NK-LN7
NK.T.cell
NK.cell
NK.like.cells
Naive.B
Neutrophil
Non.inflammatory.macrophage
Other-LN1
Other-LN2
Other-LN7
Pancreatic.A.cell
Pancreatic.D.cell
Paneth
Pericyte
Periportal.LSEC
Plasma
acinar-pancreas
angiogenic.pericyte
arterial.capillary
basal.epithelia
cDC1
cDC2
club.epithelia
cycling.EC
cycling.neuroblast
cycling.stromal
ductal-pancreas
endothelia
endothelial-appendix
epithelial2-pancreas
epithelial-1-prostate
epithelial-2-prostate
epithelial-3-prostate
epithelial-4-prostate
epithelial-5-prostate
epithelial-appendix-01
epithelial-appendix-02
epithelial-appendix-04
epithelial-colon-01
epithelial-colon-02
epithelial-colon-03
epithelial-colon-04
epithelial-ileum-01
epithelial-ileum-02
epithelial-pancreas
epithelial-stomach-01
epithelial-stomach-02
epithelial-stomach-03
epithelial-stomach-04
epithelial-stomach-05
epithelial-stomach-06
epithelial-stomach-07
epithelial-stomach-08
erythroid-liver
erythroids-bonemarrow
DC-LN10
DZ.GC.cell
Dendritic.cell
Differentiating.glia
Distal.progenitor
EECs
Endothelial
Endothelial-LN2
Endothelial-LN3
Enterocyte
Erythroid
FCRL4+.Memory.B
FDC
Fetal.arterial.EC
Fetal.venous.EC
Fibroblast
Fibroblast-LN2
FibroblasticReticular-LN3
FibroblasticReticular-LN8
GC.B.cell
Goblet.cell
Hepatocyte.A
Hepatocyte.B
Hepatocyte.C
Hepatocyte.D
Hepatocyte.E
ICC
ILC2
ILC3
ILCP
IgA.plasma.cell
IgG.plasma.cell
IgM.plasma.cell
Immature.B
Immature.pericyte
Inflammatory.macrophage
LTi.like.NCR+.ILC3
LTi.like.NCR-.ILC3
Plasma-LN2
Plasma-LN3
Plasma-LN4
Plasma-LN5
Plasma-LN7
Plasma-LN10
Plasmablast
Plasmablast-LN4
Plasmablast-LN10
Plasmacytoid.dendritic.cell
Portal.endothelial.cells
Pre.B
Pro.B
RBC
SELL+.CD4.T
SELL+.CD8.T
STAT1+.Naive.B
Stellate.cell
Stem.cells
Stromal-LN8
T-LN1
T-LN2
T-bonemarrow
T.cell.CD3.alpha.beta
T.cell.CD4
T.cell.CD8
T.cell.gamma.delta
T.cell.regulatory
T.reticular
TA
TRDV2.TRGV9.gdT
TRGV2.gdT
Tfh
Th1
Th17
Treg
Tuft
Type.B.pancreatic.cell
fibroblast
gdT
hepatocyte-01
hepatocyte-02
hepatocyte-03
hillock.epithelia
immune-T-liver
immune-appendix
immune-colon
immune-ileum
immune-liver
immune-liver-1
immune-stomach
leukocyte
luminal.epithelia
mLTo
mix-liver-1
mixed
mixedimmune-pancreas
moDC-LN2
myofibroblast
neuroendocrine.epithelia
other-1-prostate
other-2-prostate
other-bonemarrow
other-liver
pDC
pericyte-ileum-01
pericyte-ileum-02
plasma-appendix
plasma-bonemarrow
plasma-ileum
plasma-pancreas
plasma-stomach
smooth.muscle
stem-appendix
stromal-prostate
venous.capillary
b
Proportion
Section ID
c
Represented Broad Cell Type Categories by Organ
Organs
PROS
BM
LN
PANC
LIV
STO
COL
ILE
APE
Cell Counts
1e6
Broad Cell Types
Endothelial
Epithelial
Erythroid
Immune-Other
Lymphoid-B
Lymphoid-DC
Lymphoid-Other
Lymphoid-Plasma
Lymphoid-T
Mesenchymal-Stromal
Mixed
Myeloid
Neuronal-Glial
Stem

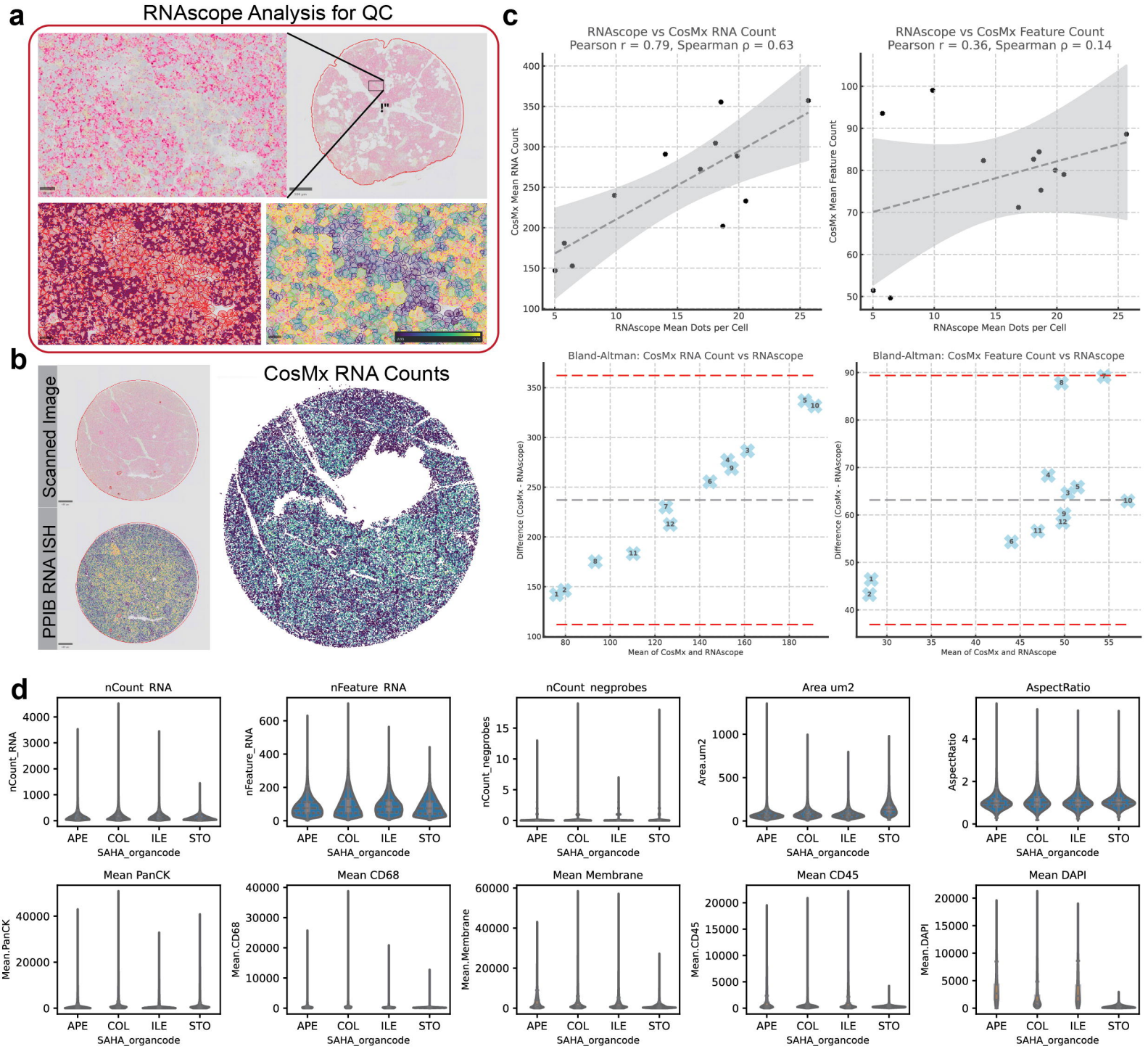
a
RNAscope Analysis for QC
b
Scanned Image
PPIB RNA ISH
CosMx RNA Counts
c
RNAscope vs CosMx RNA Count
Pearson r = 0.79, Spearman ρ = 0.63
CosMx Mean RNA Count
RNAscope Mean Dots per Cell
RNAscope vs CosMx Feature Count
Pearson r = 0.36, Spearman ρ = 0.14
CosMx Mean Feature Count
RNAscope Mean Dots per Cell
Bland-Altman: CosMx RNA Count vs RNAscope
Difference (CosMx - RNAscope)
Mean of CosMx and RNAscope
Bland-Altman: CosMx Feature Count vs RNAscope
Difference (CosMx - RNAscope)
Mean of CosMx and RNAscope
d
nCount_RNA
nFeature_RNA
nCount_negprobes
Area um2
AspectRatio
Mean PanCK
Mean CD68
Mean Membrane
Mean CD45
Mean DAPI
APE
COL
ILE
STO
SAHA_organcode

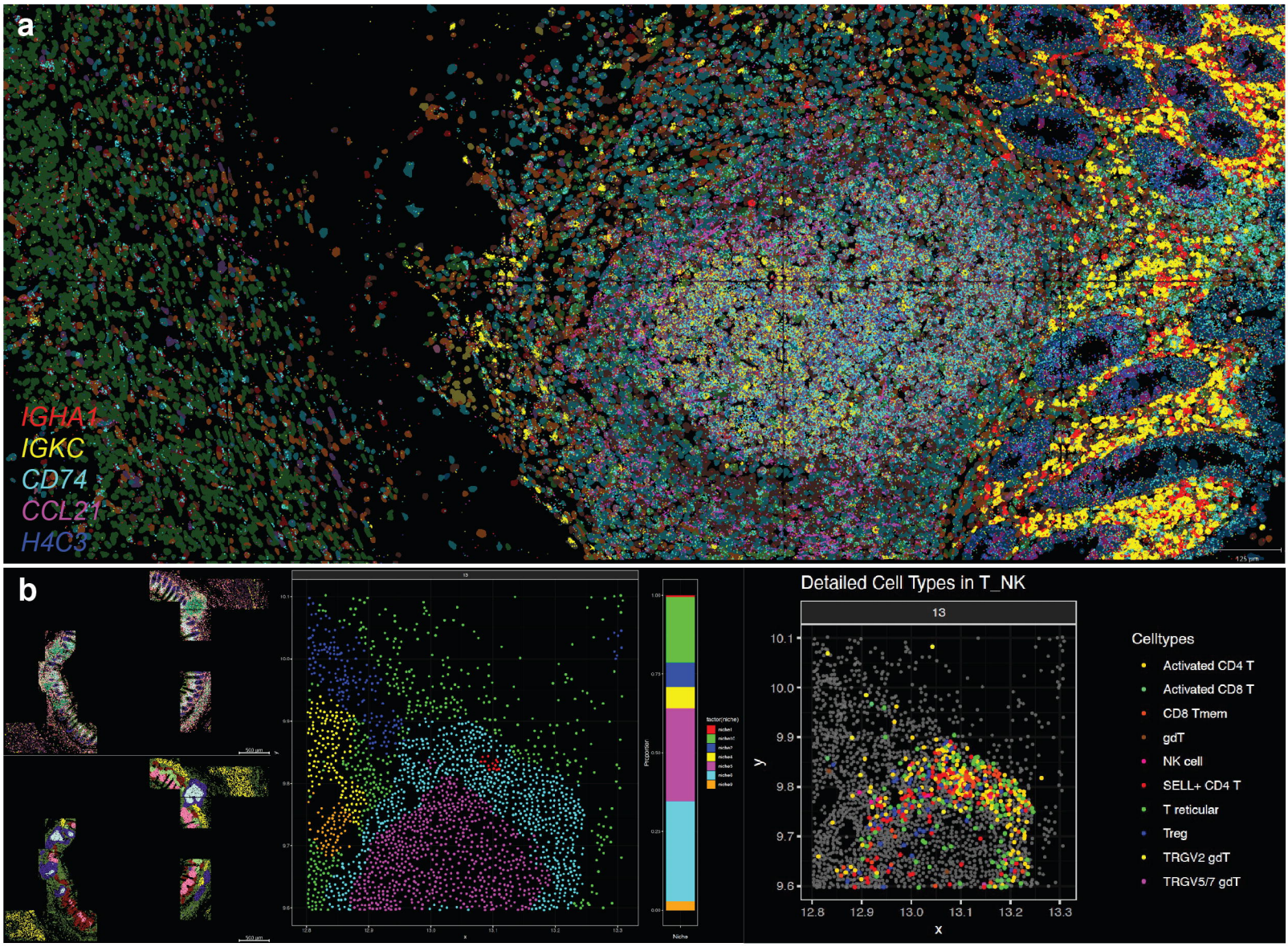
a
IGHA1
IGKC
CD74
CCL21
H4C3
125 µm
b
500 µm
13
Proportion
Niche
Detailed Cell Types in T_NK
13
y
x
Celltypes
Activated CD4 T
Activated CD8 T
CD8 Tmem
gdT
NK cell
SELL+ CD4 T
T reticular
Treg
TRGV2 gdT
TRGV5/7 gdT

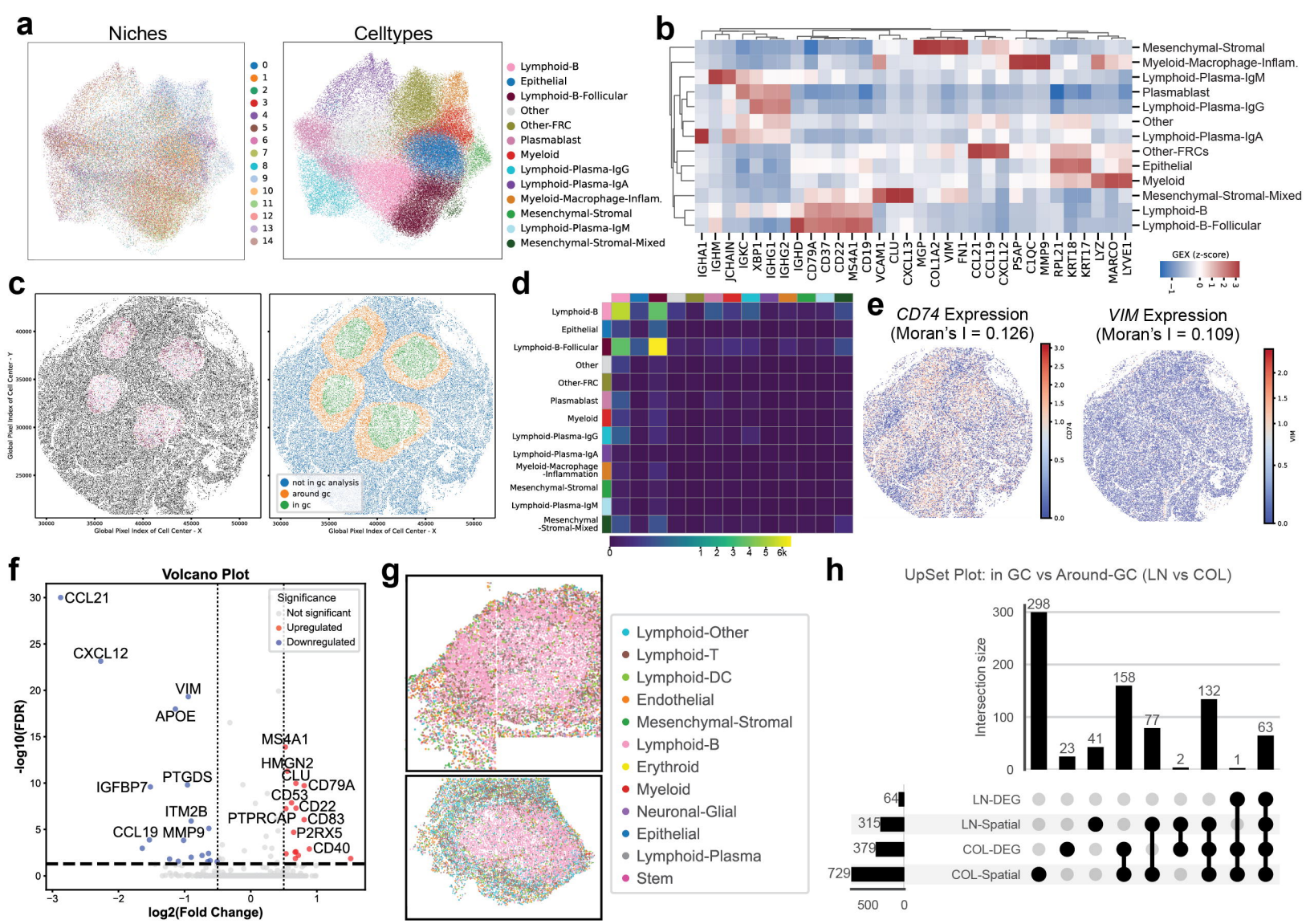
a
Niches
Celltypes
0
1
2
3
4
5
6
7
8
9
10
11
12
13
14
Lymphoid-B
Epithelial
Lymphoid-B-Follicular
Other
Other-FRC
Plasmablast
Myeloid
Lymphoid-Plasma-IgG
Lymphoid-Plasma-IgA
Myeloid-Macrophage-Inflam.
Mesenchymal-Stromal
Lymphoid-Plasma-IgM
Mesenchymal-Stromal-Mixed
b
Mesenchymal-Stromal
Myeloid-Macrophage-Inflam.
Lymphoid-Plasma-IgM
Plasmablast
Lymphoid-Plasma-IgG
Other
Lymphoid-Plasma-IgA
Other-FRCs
Epithelial
Myeloid
Mesenchymal-Stromal-Mixed
Lymphoid-B
Lymphoid-B-Follicular
IGHA1
IGHM
JCHAIN
IGKC
XBP1
IGHG1
IGHG2
IGHD
CD79A
CD37
CD22
MS4A1
CD19
VCAM1
CLU
CXCL13
MGP
COL1A2
VIM
FN1
CCL21
CCL19
CXCL12
PSAP
C1QC
MMP9
RPL21
KRT18
KRT17
LYZ
MARCO
LYVE1
GEX (z-score)
c
Global Pixel Index of Cell Center - Y
Global Pixel Index of Cell Center - X
not in gc analysis
around gc
in gc
d
Lymphoid-B
Epithelial
Lymphoid-B-Follicular
Other
Other-FRC
Plasmablast
Myeloid
Lymphoid-Plasma-IgG
Lymphoid-Plasma-IgA
Myeloid-Macrophage -Inflammation
Mesenchymal-Stromal
Lymphoid-Plasma-IgM
Mesenchymal -Stromal-Mixed
e
CD74 Expression
(Moran's I = 0.126)
VIM Expression
(Moran's I = 0.109)
f
Volcano Plot
Significance
Not significant
Upregulated
Downregulated
CCL21
CXCL12
VIM
APOE
MS4A1
HMGN2
CLU
CD79A
CD53
CD22
CD83
P2RX5
CD40
PTGDS
IGFBP7
ITM2B
CCL19
MMP9
PTPRCAP
-log10(FDR)
log2(Fold Change)
g
Lymphoid-Other
Lymphoid-T
Lymphoid-DC
Endothelial
Mesenchymal-Stromal
Lymphoid-B
Erythroid
Myeloid
Neuronal-Glial
Epithelial
Lymphoid-Plasma
Stem
h
UpSet Plot: in GC vs Around-GC (LN vs COL)
Intersection size
298
23
41
158
77
2
132
1
63
LN-DEG
LN-Spatial
COL-DEG
COL-Spatial
64
315
379
729

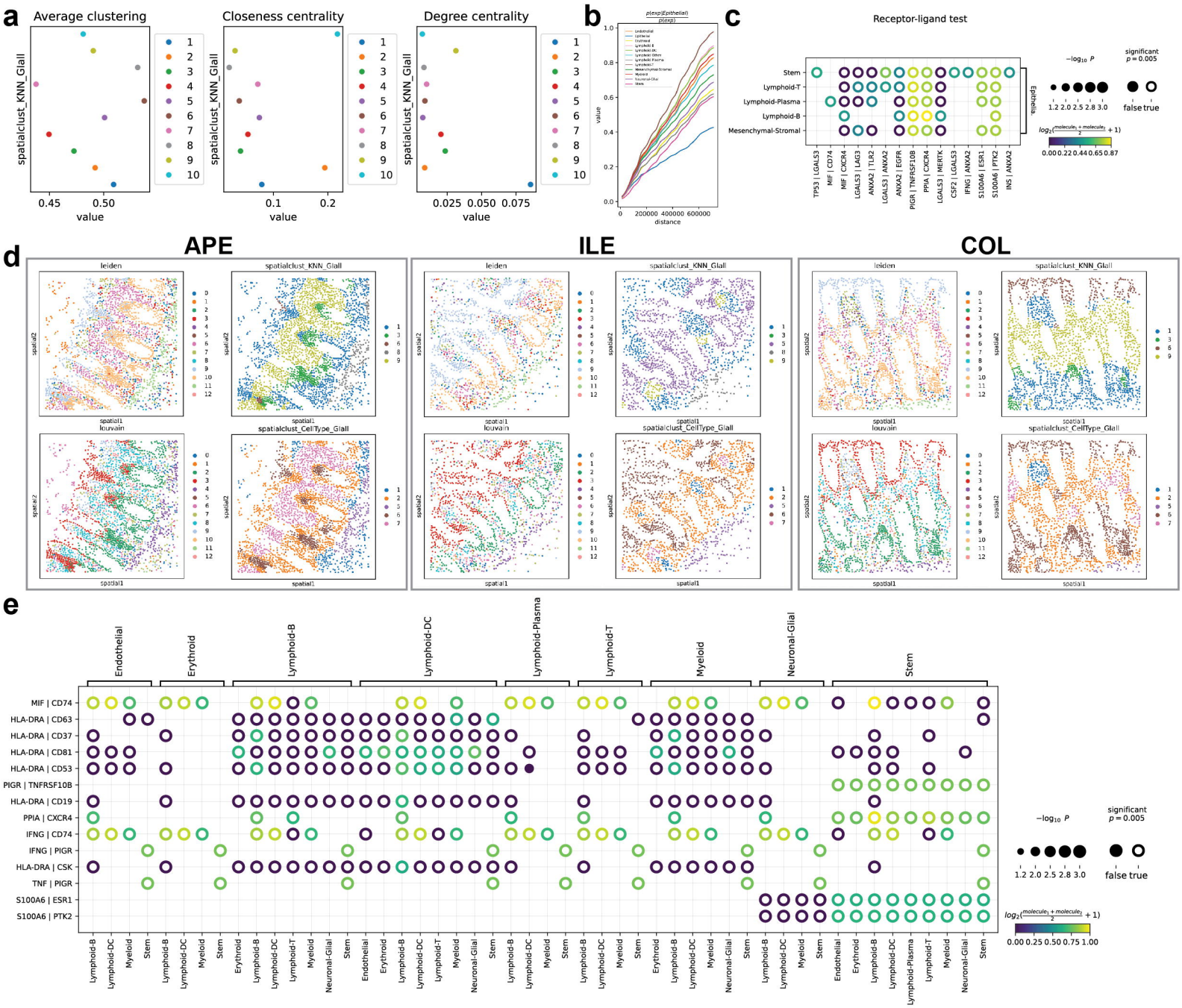
a
Average clustering
Closeness centrality
Degree centrality
spatialclust_KNN_Giall
value
b
distance
c
Receptor-ligand test
Stem
Lymphoid-T
Lymphoid-Plasma
Lymphoid-B
Mesenchymal-Stromal
Epithelia.
significant
p = 0.005
false true
d
APE
ILE
COL
leiden
louvain
spatialclust_KNN_Giall
spatialclust_CellType_Giall
e
Endothelial
Erythroid
Lymphoid-B
Lymphoid-DC
Lymphoid-Plasma
Lymphoid-T
Myeloid
Neuronal-Glial
Stem
MIF | CD74
HLA-DRA | CD63
HLA-DRA | CD37
HLA-DRA | CD81
HLA-DRA | CD53
PIGR | TNFRSF10B
HLA-DRA | CD19
PPIA | CXCR4
IFNG | CD74
IFNG | PIGR
HLA-DRA | CSK
TNF | PIGR
S100A6 | ESR1
S100A6 | PTK2
significant
p = 0.005
false true

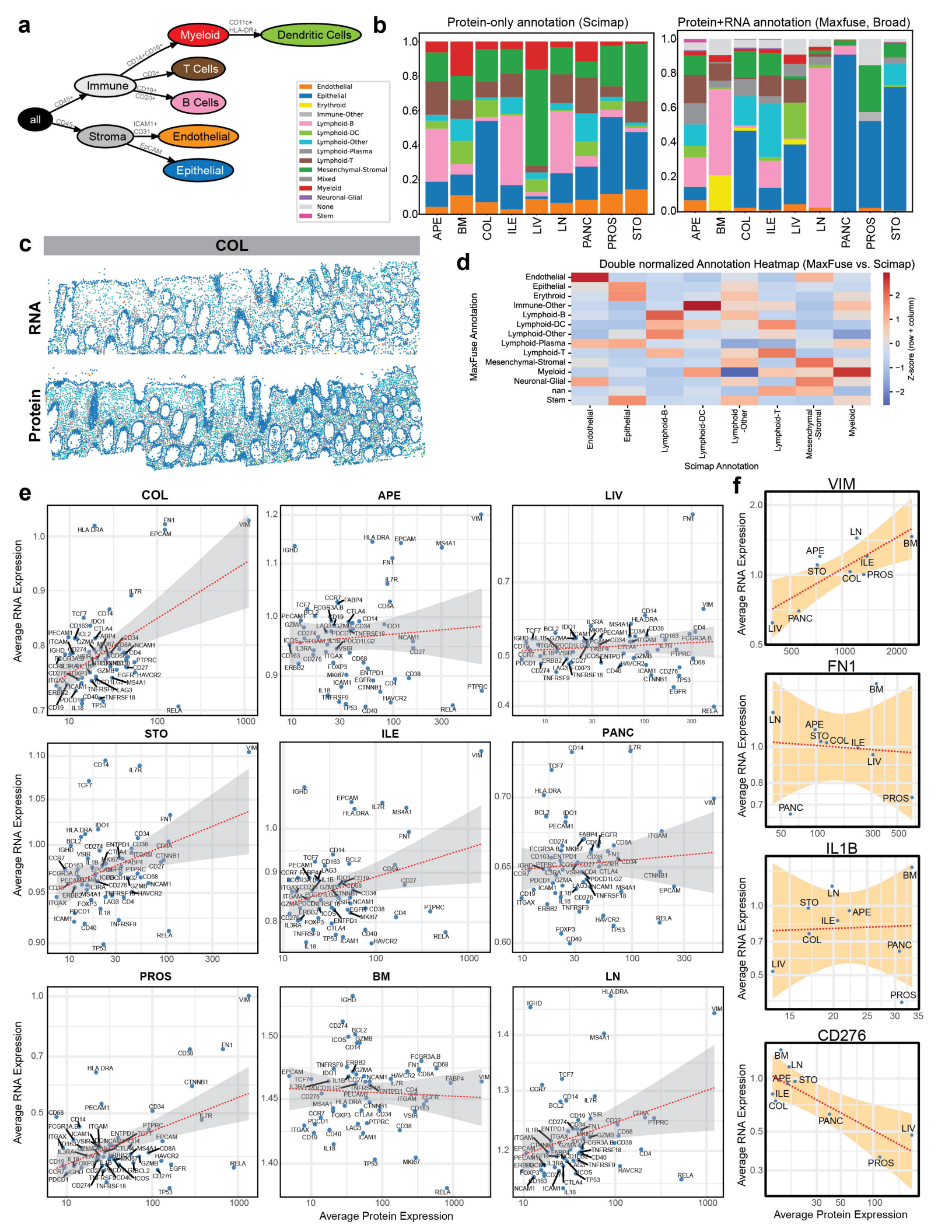
a
all
CD45+
CD45-
Immune
Stroma
CD14+CD16+
CD3+
CD19+
CD20+
CD11c+
HLA-DR+
ICAM1+
CD31+
EpCAM
Myeloid
Dendritic Cells
T Cells
B Cells
Endothelial
Epithelial
Endothelial
Epithelial
Erythroid
Immune-Other
Lymphoid-B
Lymphoid-DC
Lymphoid-Other
Lymphoid-Plasma
Lymphoid-T
Mesenchymal-Stromal
Mixed
Myeloid
Neuronal-Glial
None
Stem
b
Protein-only annotation (Scimap)
Protein+RNA annotation (Maxfuse, Broad)
APE
BM
COL
ILE
LIV
LN
PANC
PROS
STO
c
COL
RNA
Protein
d
Double normalized Annotation Heatmap (MaxFuse vs. Scimap)
MaxFuse Annotation
Scimap Annotation
Z-score (row + column)
Endothelial
Epithelial
Erythroid
Immune-Other
Lymphoid-B
Lymphoid-DC
Lymphoid-Other
Lymphoid-Plasma
Lymphoid-T
Mesenchymal-Stromal
Myeloid
Neuronal-Glial
nan
Stem
Lymphoid-Other
Mesenchymal-Stromal
e
COL
APE
LIV
STO
ILE
PANC
PROS
BM
LN
Average RNA Expression
Average Protein Expression
f
VIM
FN1
IL1B
CD276
Average RNA Expression
Average Protein Expression

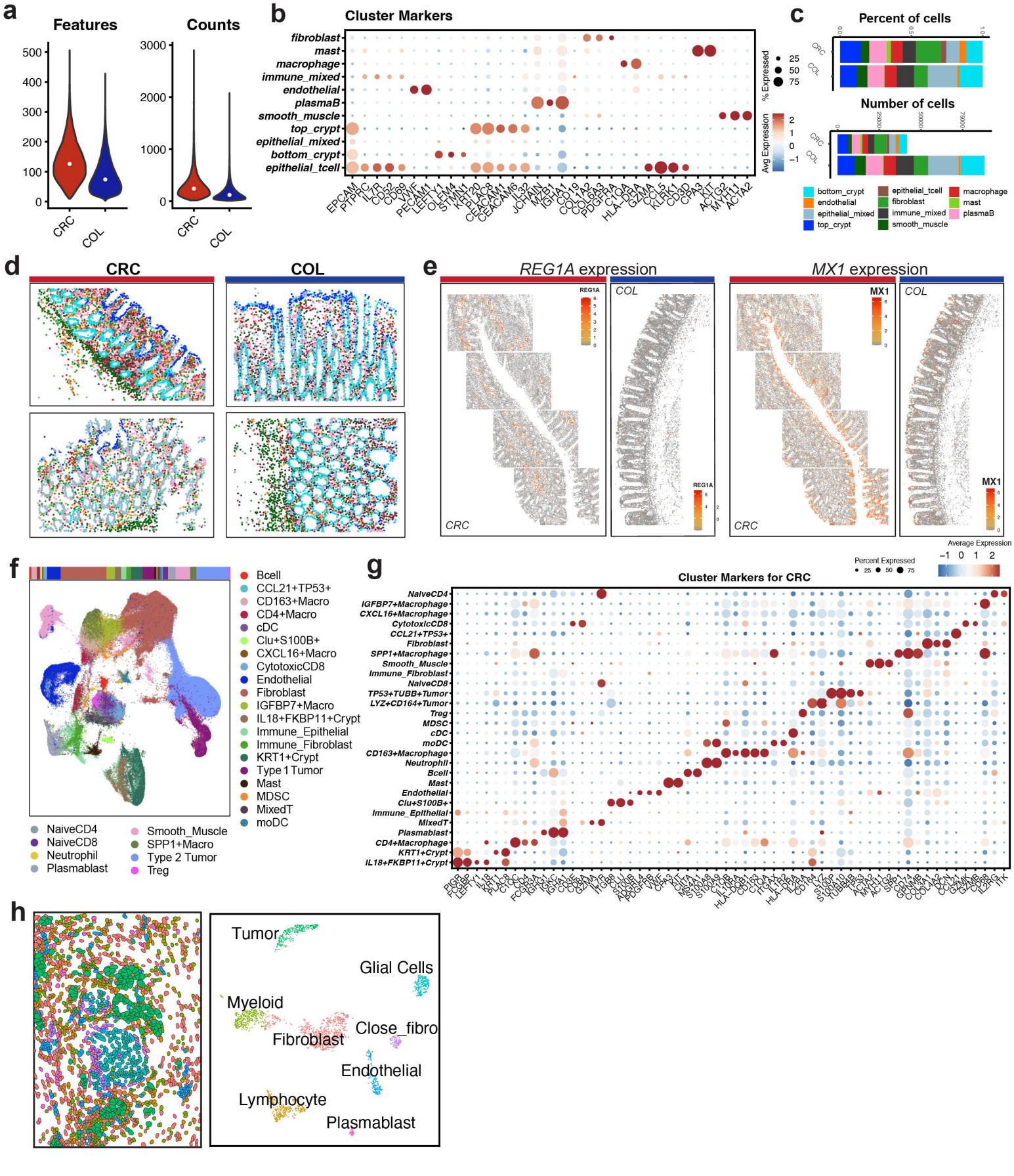
a
Features
Counts
CRC
COL
b
Cluster Markers
fibroblast
mast
macrophage
immune_mixed
endothelial
plasmaB
smooth_muscle
top_crypt
epithelial_mixed
bottom_crypt
epithelial_tcell
% Expressed
Avg Expression
c
Percent of cells
Number of cells
bottom_crypt
endothelial
epithelial_mixed
top_crypt
epithelial_tcell
fibroblast
immune_mixed
smooth_muscle
macrophage
mast
plasmaB
d
CRC
COL
e
REG1A expression
MX1 expression
CRC
COL
f
Bcell
CCL21+TP53+
CD163+Macro
CD4+Macro
cDC
Clu+S100B+
CXCL16+Macro
CytotoxicCD8
Endothelial
Fibroblast
IGFBP7+Macro
IL18+FKBP11+Crypt
Immune_Epithelial
Immune_Fibroblast
KRT1+Crypt
Type 1 Tumor
Mast
MDSC
MixedT
moDC
NaiveCD4
NaiveCD8
Neutrophil
Plasmablast
Smooth_Muscle
SPP1+Macro
Type 2 Tumor
Treg
g
Cluster Markers for CRC
Percent Expressed
Average Expression
h
Tumor
Glial Cells
Myeloid
Close_fibro
Fibroblast
Endothelial
Lymphocyte
Plasmablast

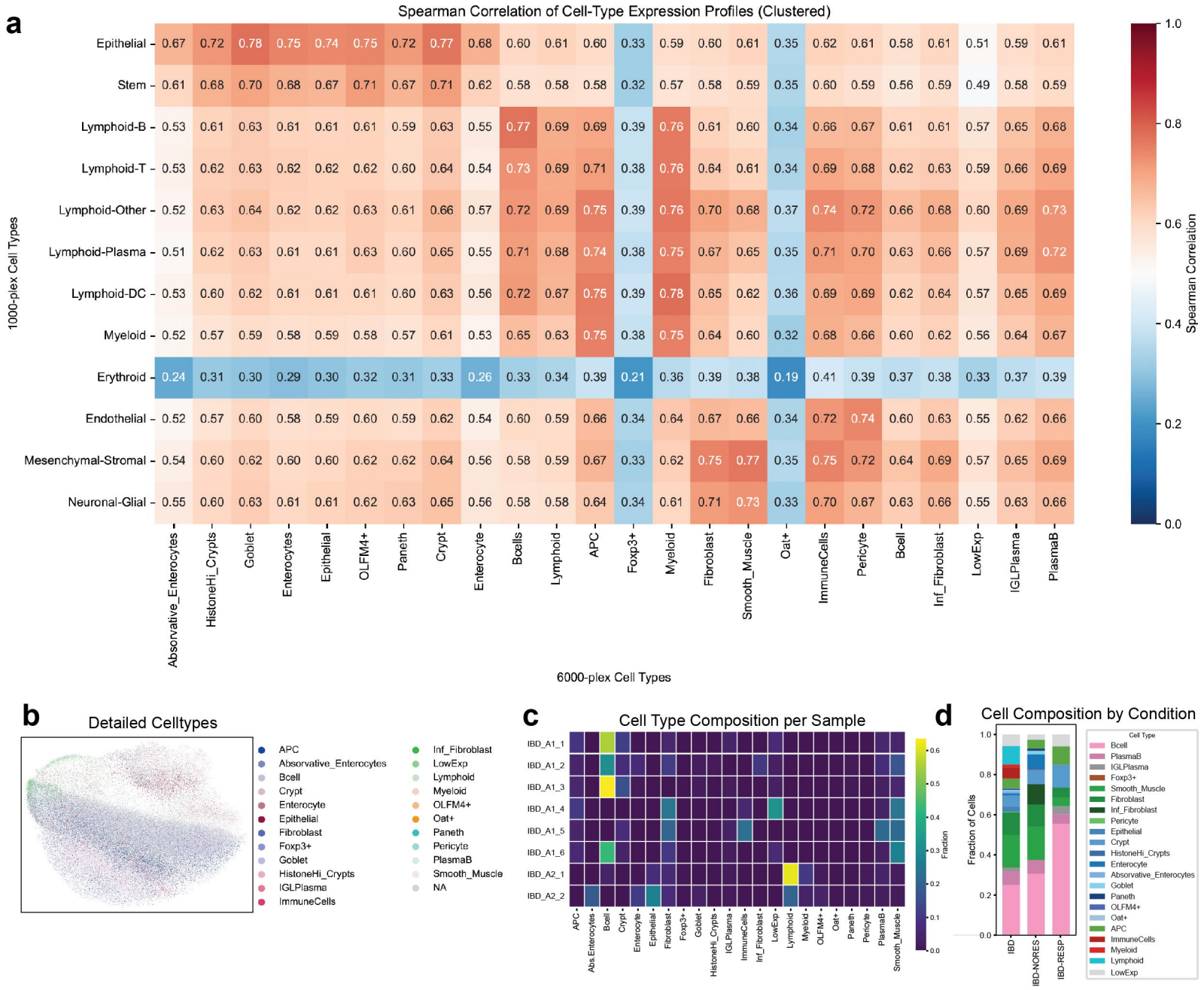
a
Spearman Correlation of Cell-Type Expression Profiles (Clustered)
1000-plex Cell Types
6000-plex Cell Types
Spearman Correlation
Epithelial
Stem
Lymphoid-B
Lymphoid-T
Lymphoid-Other
Lymphoid-Plasma
Lymphoid-DC
Myeloid
Erythroid
Endothelial
Mesenchymal-Stromal
Neuronal-Glial
Absorvative_Enterocytes
HistoneHi_Crypts
Goblet
Enterocytes
Epithelial
OLFM4+
Paneth
Crypt
Enterocyte
Bcells
Lymphoid
APC
Foxp3+
Myeloid
Fibroblast
Smooth_Muscle
Oat+
ImmuneCells
Pericyte
Bcell
Inf_Fibroblast
LowExp
IGLPlasma
PlasmaB
b
Detailed Celltypes
APC
Absorvative_Enterocytes
Bcell
Crypt
Enterocyte
Epithelial
Fibroblast
Foxp3+
Goblet
HistoneHi_Crypts
IGLPlasma
ImmuneCells
Inf_Fibroblast
LowExp
Lymphoid
Myeloid
OLFM4+
Oat+
Paneth
Pericyte
PlasmaB
Smooth_Muscle
NA
c
Cell Type Composition per Sample
IBD_A1_1
IBD_A1_2
IBD_A1_3
IBD_A1_4
IBD_A1_5
IBD_A1_6
IBD_A2_1
IBD_A2_2
Fraction
d
Cell Composition by Condition
Fraction of Cells
IBD
IBD-NORES
IBD-RESP
Cell Type